Monthly Notices of the ROYAL ASTRONOMICAL SOCIETY

MNRAS **512,** 265–284 (2022) https://doi.org/10.1093/mnras/stac210
Advance Access publication 2022 February 4

Mysterious odd radio circle near the large magellanic cloud – an intergalactic supernova remnant?

Miroslav D. Filipović [1]★ J. L. Payne [1] R. Z. E. Alsaberi [1] R. P. Norris [1,2] P. J. Macgregor [1] L. Rudnick [3] B. S. Koribalski [1,2] D. Leahy [4] L. Ducci,[5,6] R. Kothes,[7] H. Andernach [8] L. Barnes,[1] I. S. Bojičić,[1] L. M. Bozzetto,[1] R. Brose,[9,10] J. D. Collier [1,11] E. J. Crawford [1] R. M. Crocker [12] S. Dai [1] T. J. Galvin [13] F. Haberl,[14] U. Heber,[15] T. Hill,[1] A. M. Hopkins,[1,16] N. Hurley-Walker,[13] A. Ingallinera [17] T. Jarrett [1,18] P. J. Kavanagh [19] E. Lenc [2] K. J. Luken [1,2] D. Mackey [12] P. Manojlović,[1] P. Maggi,[20] C. Maitra [14] C. M. Pennock [21] S. Points,[22] S. Riggi [17] G. Rowell,[23] S. Safi-Harb,[24] H. Sano [25] M. Sasaki [15] S. Shabala [26] J. Stevens,[2] J. Th. van Loon,[21] N. F. H. Tothill,[1] G. Umana,[17] D. Urošević,[27,28] V. Velović,[1] T. Vernstrom [2] J. L. West [29] and Z. Wan [30]

Affiliations are listed at the end of the paper

Accepted 2022 January 20. Received 2022 January 11; in original form 2021 September 21

ABSTRACT

We report the discovery of J0624–6948, a low-surface brightness radio ring, lying between the Galactic Plane and the large magellanic cloud (LMC). It was first detected at 888 MHz with the Australian Square Kilometre Array Pathfinder (ASKAP), and with a diameter of ∼196 arcsec. This source has phenomenological similarities to odd radio circles (ORCs). Significant differences to the known ORCs – a flatter radio spectral index, the lack of a prominent central galaxy as a possible host, and larger apparent size – suggest that J0624–6948 may be a different type of object. We argue that the most plausible explanation for J0624–6948 is an *intergalactic supernova remnant* due to a star that resided in the LMC outskirts that had undergone a single-degenerate type Ia supernova, and we are seeing its remnant expand into a rarefied, intergalactic environment. We also examine if a massive star or a white dwarf binary ejected from either galaxy could be the supernova progenitor. Finally, we consider several other hypotheses for the nature of the object, including the jets of an active galactic nucleus (30Dor) or the remnant of a nearby stellar super-flare.

Key words: stars: flare – ISM: supernova remnants – galaxies: jets – Magellanic Clouds – radio continuum: general.

1 INTRODUCTION

A new generation of radio telescopes is revealing new features of the radio Universe, due to the combined effects of high-sensitivity, good spatial sampling, and wide area coverage. Rare, low surface brightness features are now more easily detected, as demonstrated by the recent emergence of the class of ring-shaped radio sources known as odd radio circles (ORCs; Koribalski et al. 2021; Norris et al. 2021b). Radio sources often have circular features that can represent nearly spherical objects, including supernova remnants (SNRs), planetary nebulae (PN), (super)bubbles, H II regions, circumstellar shells or disc-like objects, protoplanetary discs and star-forming galaxies, or even ring-shaped imaging artefacts.

While ORCs resemble SNRs in some respects, the two populations seem to be distinct. Most known Galactic and magellanic clouds (MCs) SNRs are radio emitters. However, detections in the optical and X-ray frequencies have been increasingly noted in recent times (Millar, White & Filipović 2012; Bozzetto et al. 2017). SNR outliers remind us that they are not a monolithic population. Supernova (SN) progenitors, in different interstellar medium (ISM) and at different evolutionary stages, produce unique shapes in individual objects. This includes a population of so-called host-less (intergalactic) SNe, discovered beyond our local group (LG) of galaxies, which cannot be associated to any galaxy (Zinn, Grunden & Bomans 2011). However, thus far no such SN, nor their remnants, have been seen in our LG.

These host-less intergalactic SNe may come from hyper or high velocity runaway stars (Zinn et al. 2011), producing a remnant whose velocity will be modulated by a SN kick (Boubert et al. 2017; Evans, Renzo & Rossi 2020; Evans et al. 2021). This scenario could have some exotic consequences, such as runaway pulsars and SNe far from star-forming regions, including the old/outer stellar disc of galaxies such as the MCs or Milky Way (MW). At the same time, galaxy haloes and outer discs harbour stars that also explode, though mainly as type Ia SNe (Hakobyan et al. 2017).

First detected at 888 MHz with the Australian Square Kilometre Array Pathfinder (ASKAP), J0624–6948 is located between the large magellanic cloud (LMC) and the plane of the MW (Figs 1 and 2). We present a multifrequency study and an analysis of J0624–6948. While we argue for an intergalactic SNR scenario, we also consider several other hypotheses for the nature of the object, including jets of an 30Dor or the remnant of a nearby stellar super-flare.

★ E-mail: m.filipovic@uws.edu.au

© 2022 The Author(s)
Published by Oxford University Press on behalf of Royal Astronomical Society

Downloaded from https://academic.oup.com/mnras/article/512/1/265/6522201 by UNI CATANIA FAC AGRARIA user on 27 February 2025

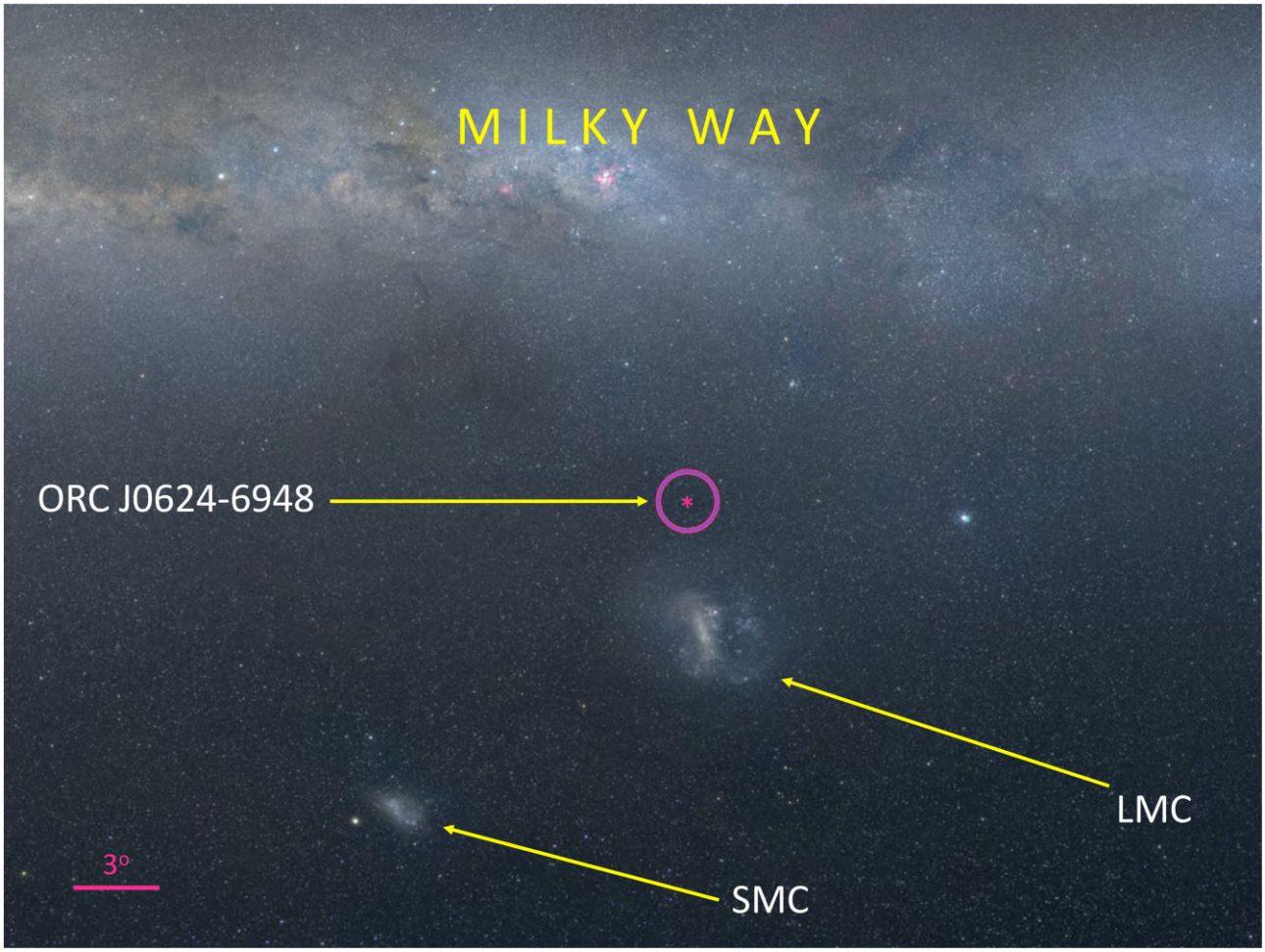

Figure 1. Optical image of the sky around J0624–6948. The position of J0624–6948 (small object at the centre of the purple ring indicated by ∗) is indicated with respect to the MW galactic plane, the LMC and the small magellanic cloud (SMC). Optical image credit: Axel Mellinger, Central Michigan University.

2 OBSERVATIONS AND DATA REDUCTION

2.1 Radio imaging

2.1.1 ASKAP data

J0624–6948 was originally detected in June 2019 as a part of the ASKAP Early Science Project (Pennock et al. 2021). The data were processed using the ASKAPsoft pipeline, including multifrequency synthesis imaging, multiscale clean, and self-calibration (Norris et al. 2021b). The 888 MHz ASKAP image shown in Figs 2 and 3 (top row left) has a sensitivity of $\sigma = 58\,\mu\mathrm{Jy\,beam^{-1}}$ and a synthesized beam of 13.87 × 12.11 arcsec at the beam parallactic angle of −84.4 degrees.

2.1.2 ATCA data

Follow-up observations were obtained with various ATCA arrays at 2232, 5500, and 9000 MHz (Table 1) and images are shown in Fig. 3. We used the source PKS B1934–638 as a primary calibrator (bandpass and flux density) and the source PKS B0530–727 as a phase calibrator for all observing sessions (Table 1).

The MIRIAD (Sault, Teuben & Wright 1995) and KARMA (Gooch 1995) software packages were used to reduce, compare, and analyse the data. We combine observations of various interferometer arrays to a common *uv*-plane for each of the three frequency bands. Given that our object of interest is diffuse and of low surface brightness, we experimented with the range of various values for weighting and tapering. To maximize and enhance source diffuse emission, we found that a Briggs weighting robust parameter of 1 (closer to natural weighting) is the most optimal choice. Also, an additional 7 arcsec Gaussian taper is included to further enhance the diffuse emission. This allows us to achieve resolutions of full width at half-maximum of 15 × 15 arcsec, 10 × 10 arcsec, and 10 × 10 arcsec for the 2232, 5500, and 9000 MHz images, respectively. All images were corrected for the primary beam attenuation. The rms noise (or 1σ) is $20\,\mu\mathrm{Jy\,beam^{-1}}$ for the 2232 MHz image, $5\,\mu\mathrm{Jy\,beam^{-1}}$ for the 5500 MHz image, and $7\,\mu\mathrm{Jy\,beam^{-1}}$ for the 9000 MHz image. The rms numbers quoted in this paper represent noise level at the image centre and because of the primary beam response correction the noise increases towards the edges of the image. Given our observing frequencies and arrays *uv* coverage, the maximum angular scale that the image is sensitive to ranges from 49 arcmin (for ASKAP) to 6 and 3.5 arcmin for ATCA 5500 and 9000 MHz images.

In order to further enhance the signal-to-noise ratio, we averaged the 2232, 5500, and 9000 MHz maps (Fig. 3) by extrapolating each of them to 888 MHz using a spectral index (defined by $S \propto \nu^{\alpha}$, where S is flux density, ν is the frequency, and α is the spectral index) of $\alpha = -0.4$ as we determined for the spectral index (Section 3). We convolved all these maps to 15 arcsec, as well as subtracting four-point sources from the south-west region (see Table 2). As a result,

Downloaded from https://academic.oup.com/mnras/article/512/1/265/6522201 by UNI CATANIA FAC AGRARIA user on 27 February 2025

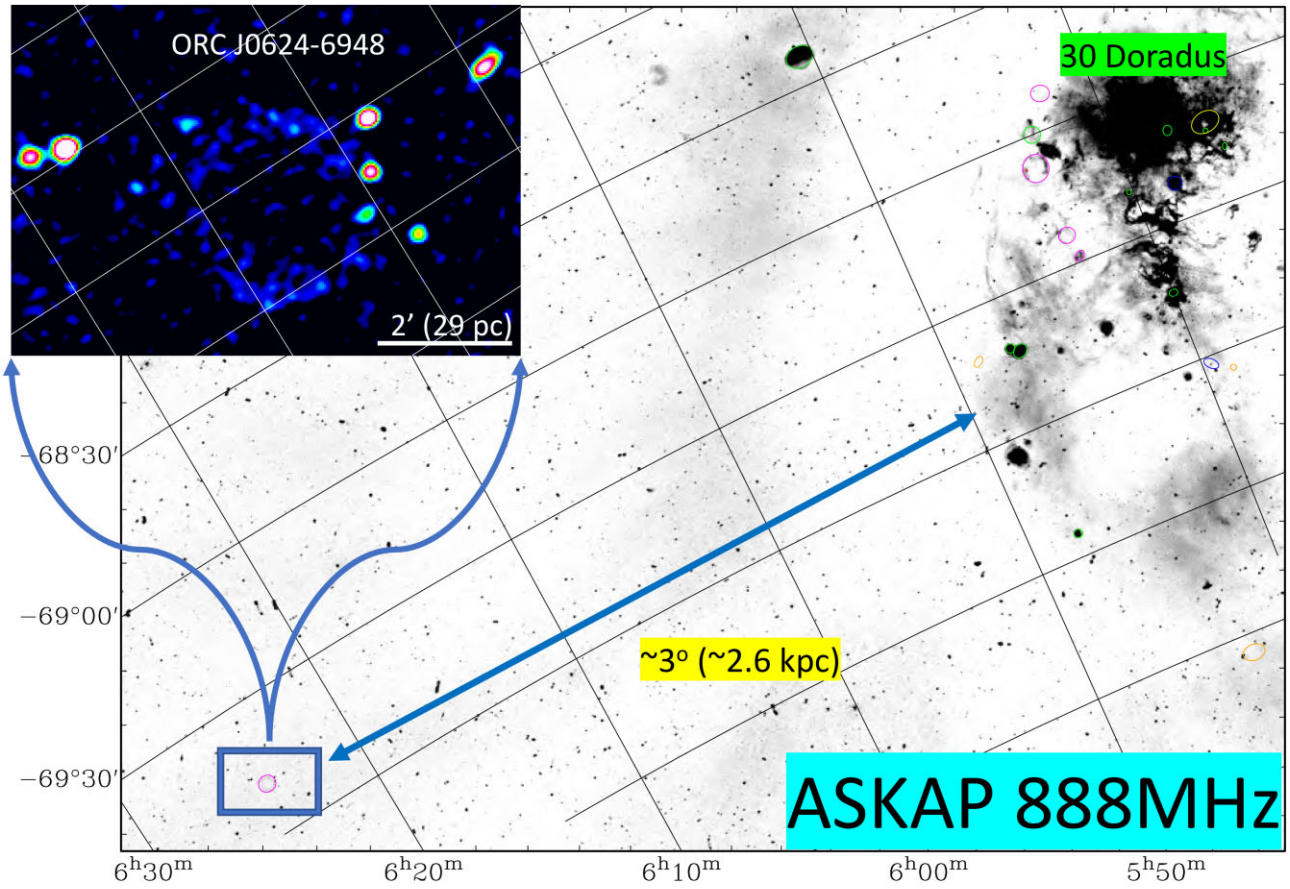

Figure 2. ASKAP 888 MHz image with J0624–6948 in the lower left and the LMC in the upper right. The various coloured circles/ellipses represent the positions of known LMC SNRs and SNR candidates (Bozzetto et al. 2017). The separation of ∼2.6 kpc indicated here assumes that J0624–6948 is at the same distance as the LMC (50 kpc). The inset in the upper left is zoomed in J0624–6948 at ASKAP native frequency of 888 MHz.

the 888 MHz, the extrapolated 2232 MHz, and the extrapolated 5500 MHz maps have all the same noise of ∼400 mK, while the 9000 MHz map has a much higher value ∼2 K. Thus, we averaged the three lower frequencies together; the combined map's noise is a factor of two lower than that of the ASKAP 888 MHz map alone. Hereafter, we refer to this combined frequency image as the 'effective 10-cm' (at a weighted frequency of 3623 MHz) map. Finally, a map emphasizing the diffuse emission (Fig. 4; top left) was created by adding the effective 10-cm map at 15 arcsec resolution to an image of the large-scale emission alone, at a resolution of 35 arcsec, in the ratio of 0.3–0.7. The large-scale emission image was created by filtering out all of the small-scale emission using the multiresolution filtering technique of Rudnick (2002), using a box size of 45 arcsec. Note that since this image is at two different resolutions, it is useful for visualization only, and is not used quantitatively in the paper.

2.2 X-ray imaging

The sky region around J0624–6948 was observed serendipitously by *XMM-Newton* on 2020 March 14–15. Data were reduced and analysed using standard routines in the Science Analysis System (SAS; version 19.0.0) and calibration files. We used only data from the European Photon Imaging Camera (EPIC) instruments that are equipped with CCDs based on Metal Oxide Semi-conductor technology (MOS1 and MOS2, Turner et al. 2001), as J0624–6948 was outside the field of view of EPIC-pn (Strüder et al. 2001), which was operated in small window read-out mode. After filtering the data for high background contamination, the net exposure times are ∼85.62 and ∼85.60 ks for MOS1 and MOS2, respectively (see *XMM-Newton* image in Fig. 5).

2.3 Other images

We searched for a possible counterpart using Parkes GASS/HI4PI data, as well as SkyMapper (Onken et al. 2019), The Two Micron All-Sky Survey (2MASS), Wide-Field Infrared Survey Explorer (WIFES), and Survey of the MAgellanic Stellar History (SMASH) data in optical/IR wavebands. The WIFES imaging was custom constructed to preserve the native angular resolution (∼6 arcsec in the W1 band; Jarrett et al. 2012). Details about GASS/HI4PI observation can be found in HI4PI Collaboration (2016) and SMASH data in Nidever et al. (2021; see Fig. 5). We also searched other available catalogues and surveys including Murchison Widefield Array images (For et al. 2018), the *Planck* free–free emission maps (Crawford et al. 2016) and *Fermi-LAT* 4FGL and 3FHL GeV gamma-ray source catalogues (Ajello et al. 2020).

3 PROPERTIES OF J0624–6948

The apparent location of J0624–6948 is between the LMC and the plane of the MW, about 3° (∼2.6 kpc at the distance of the LMC of 50 kpc; Pietrzyński et al. 2019) east of the LMC's radio contin-

Downloaded from https://academic.oup.com/mnras/article/512/1/265/6522201 by UNI CATANIA FAC AGRARIA user on 27 February 2025

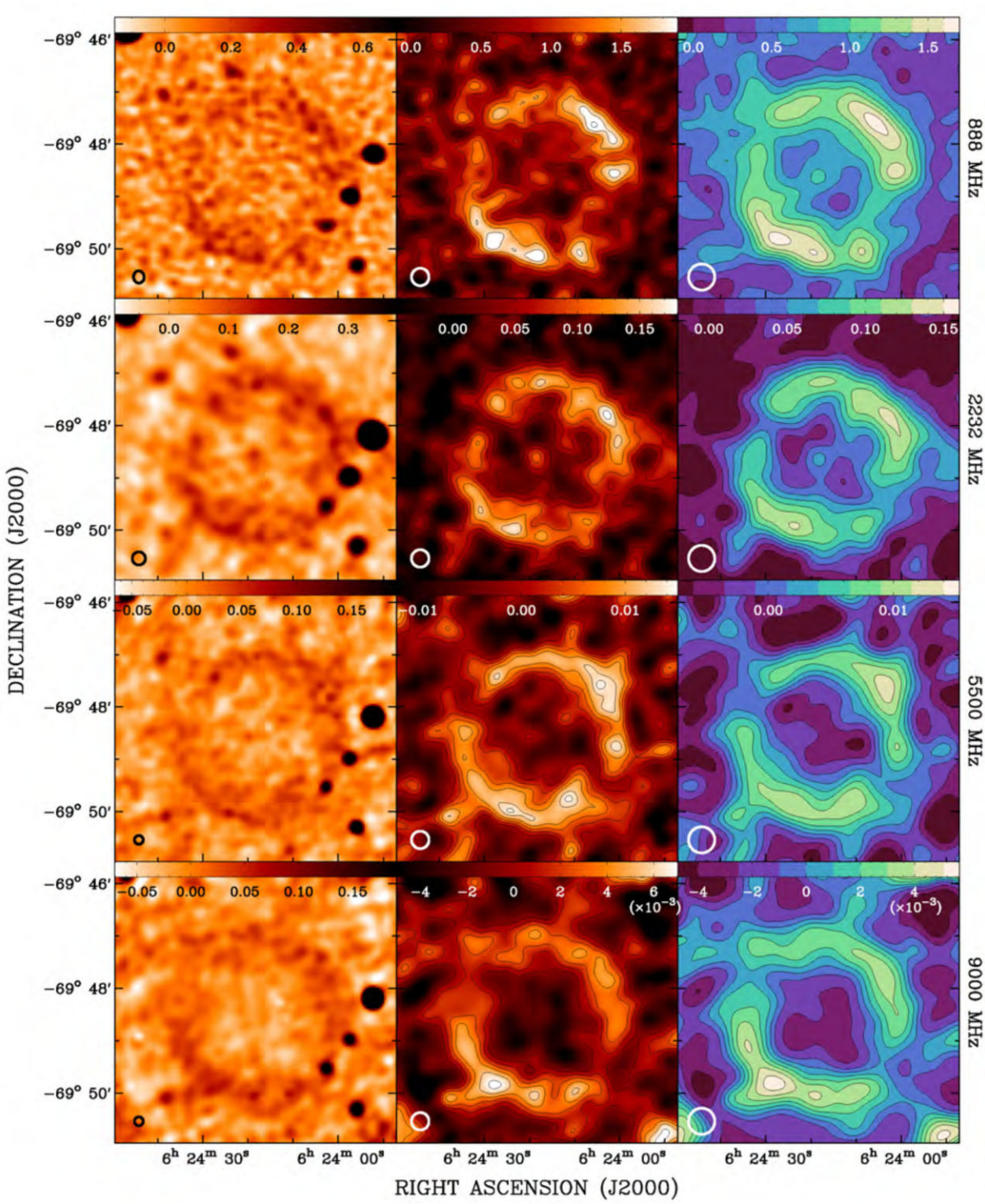

Figure 3. Radio continuum images of J0624–6948 obtained with (first row; left) ASKAP at 888 MHz (σ = 60 μJy beam^{-1}), (second row; left) Australia Telescope Compact Array (ATCA) at 2232 MHz (σ = 20 μJy beam^{-1}), (third row; left) ATCA at 5500 MHz (σ = 10 μJy beam^{-1}), and (fourth row; left) ATCA at 9000 MHz (σ = 7 μJy beam^{-1}). The images in the left column are with a native synthesized beam (black circle, or in the case of the ASKAP image a black ellipse, in the bottom left corner) of 13.87 × 12.11 arcsec^2, 15 × 15 arcsec^2, 10 × 10 arcsec^2, and 10 × 10 arcsec^2 for 888, 2232, 5500, and 9000 MHz, respectively. The intensity scale bars on top of each image are labelled in mJy beam^{-1}. For the images in the middle and right column, we subtracted the four nearby point sources (see Table 2) and smoothed to 20 and 30 arcsec resolution, respectively (white circle in the bottom left corner). The intensity scale bars on top of these images are in brightness temperature (K_{Tb}).

Downloaded from https://academic.oup.com/mnras/article/512/1/265/6522201 by UNI CATANIA FAC AGRARIA user on 27 February 2025

Table 1. ATCA observations centred on J0624–6948 used here to create images at 2232, 5500, and 9000 MHz.

Date	Array Config.	Project Code	Frequency (MHz)	Int. time (Min)
12-12-2019	1.5C	CX450	2232	265
26-01-2020	6A	C3296	2232	196
23-02-2020	367	C3292	2232	74
23-02-2020	367	C3292	5500, 9000	74
15-03-2020	6D	C3295	2232	119
15-03-2020	6D	C3295	5500, 9000	118
28-03-2020	H168	CX310	2232	87
28-03-2020	H168	CX310	5500, 9000	87
12-04-2020	6A	C3330	5500, 9000	235
10-06-2020	1.5C	CX454	5500, 9000	355
30-10-2020	6B	CX310	2232	177
30-10-2020	6B	CX310	5500, 9000	177
09-02-2021	750C	C3383	2232	98
09-02-2021	750C	C3383	5500, 9000	108

uum eastern edges (RA(J2000) = $05^h50^m00^s$ and Dec(J2000) = $-70°00'00''$; Filipović et al. 2021) and in the direction towards the MW (Figs 1 and 2). The geometric centre of J0624–6948 (determined as described in Kavanagh et al. (2016), Kavanagh et al. (2021)) is located at RA(J2000) = $06^h24^m17.78^s$ and Dec(J2000) = $-69°48'37.8''$ (ΔRA and ΔDec ∼2 arcsec; Galactic coordinates: $l = 280.168°$ and $b = -27.662°$). A red-green-blue colour-composite image of J0624–6948, consisting of optical (R), radio (G), and X-ray (B) observations is shown in Fig. 5.

3.1 Flux density and spectral index

For the J0624–6948 flux density measurements, we used the method described in Hurley-Walker et al. (2019b, section 2.4). After careful region selection that excludes all obvious point sources, the total radio flux density measured for J0624–6948 is 11.7 ± 5.8 mJy at 888 MHz, 9.1 ± 3.5 mJy at 2232 MHz, 4.5 ± 1.9 mJy at 5500 MHz, and 3.6 ± 1.8 mJy at 9000 MHz. This gives a spectral index of $\alpha = -0.54 \pm 0.08$ (Table 2). The large error in flux density measurements is due to the low surface brightness of J0624–6948. Flux densities of four point sources, in each band, were estimated using the AEGEAN Source Finding suite of tools (Hancock, Trott & Hurley-Walker 2018) with default parameters. They are excluded from the estimate of J0624–6948 total flux.

We also produced a spectral index map for J0624–6948 using 888, 2232, 5500, and 9000 MHz images. First, the images were smoothed to their lowest angular resolution (15 arcsec) using MIRIAD task CONVOL, then they were re-gridded using MIRIAD task REGRID. The MIRIAD task MATHS was used to create the spectral index map from these data as shown in Fig. 6. We find that the observed α varies from $-0.40 > \alpha > -0.75$ with a typical uncertainty of $\Delta\alpha = 0.19$. Thus, there is no evidence for spectral index variations across J0624–6948.

We detect a weak (∼4σ) point-like central radio source at RA(J2000) = $06^h24^m18.7^s$ and Dec(J2000) = $-69°48'34.3''$. The integrated flux density of this source is: $S_{888} = 210 \pm 20\ \mu$Jy, $S_{2232} = 125 \pm 15\ \mu$Jy, and $S_{5500} = 31 \pm 5\ \mu$Jy, leading to a spectral index of $\alpha = -1.03 \pm 0.25$ (Table 2). Given such a steep spectral index, this central radio source is unlikely a Pulsar Wind Nebula (PWN; Reynolds, Gaensler & Bocchino 2012). It is consistent with being a pulsar or central 30Dor engine of J0624–6948 (Fig. 5). However, it is located 10.8 arcsec away from the geometrical centre of J0624–6948. At the location of the 5500 MHz radio source, we find in SMASH (optical) images a faint galaxy ($r = 22.38$ mag), which makes this source very unlikely to be a pulsar or PWN. Based on these optical images, J0624–6948 could either be an edge-on late-type or lenticular (S0) galaxy (Fig. 5, left inset). The optical faintness of this galaxy, together with an expected small Galactic extinction (A_r ∼0.17 mag; Schlafly & Finkbeiner (2011)), leads us to estimate its redshift as $z \gtrsim 0.7$. This redshift was estimated using the ANNz2 (Sadeh, Abdalla & Lahav 2016) algorithm and the k-Nearest Neighbours algorithm described in Luken et al. (2022, in preparation) using the SMASH g, r, i, and z magnitudes and AllWISE W1-W4 magnitudes. Given the lack of similar optical data to use as a training set for the models, we hesitate to put a firm estimate on the redshift, and instead provide a cautious lower limit.

Nearby point and point-like radio sources marked in Fig. 5 have spectral indices typical for background objects, as can be seen from a small group of four radio sources towards the south-west edges of the J0624–6948 ring (Table 2 and Fig. 8). There is no obvious connection or association of these sources with the extended ring-like structure of J0624–6948. We classify ASKAP J062352.3–694813.2 as a GPS source (Collier et al. 2018) with a turnover frequency at ∼4900 MHz. ASKAP J062357.3–694857.8 is a typical background radio source with $\alpha = -0.79 \pm 0.03$. The spectral indices of the other two sources (ASKAP J062402.6–694932.8 and ASKAP J062355.8–695016.8) suggest a dominantly thermal nature or possible variable radio sources.

We tried to confirm the spectral index of J0624–6948 by producing TT-plots (Turtle et al. 1962) between the radial profiles of the source at different frequencies. This proved to be very effective to properly determine the spectral index of a steep spectrum source located on top of a diffuse flat spectrum source (Kothes et al. 2020). TT-plots should therefore give more reliable results for observations that may suffer from missing short spacings, which in essence cause a diffuse negative source. If the observations suffer from missing short spacings, it would then produce an offset from the origin of the diagram.

Table 2. Flux density and spectral index estimates for J0624–6948, central source (J062418.1–694834.3), and four bright sources near the south-west rim. These four sources are possibly background objects that may not be related to J0624–6948. Source J062352.3–694813.2 is classified as a Gigahertz Peak Spectrum (GPS) and with no power law spectrum as such, we did not estimate the spectral index as for the other sources.

Source Name ASKAP	RA (J2000) (h m s)	Dec. (J2000) (° ′ ″)	$S_{888\,MHz}$ (mJy)	$S_{2232\,MHz}$ (mJy)	$S_{5500\,MHz}$ (mJy)	$S_{9000\,MHz}$ (mJy)	$\alpha \pm \Delta\alpha$
J0624–6948	06 24 17.78	−69 48 37.8	11.7 ± 5.8	9.1 ± 3.5	4.5 ± 1.9	3.6 ± 1.8	−0.54 ± 0.08
J062418.1–694834.3	06 24 18.17	−69 48 34.3	0.21 ± 0.02	0.125 ± 0.015	0.031 ± 0.005	–-	−1.03 ± 0.25
J062352.3–694813.2	06 23 52.32	−69 48 13.2	4.06 ± 0.06	10.51 ± 0.05	15.49 ± 0.03	12.41 ± 0.04	GPS
J062357.3–694857.8	06 23 57.35	−69 48 57.8	2.19 ± 0.06	1.16 ± 0.05	0.53 ± 0.03	0.36 ± 0.04	−0.79 ± 0.02
J062402.6–694932.8	06 24 02.61	−69 49 32.8	0.83 ± 0.09	0.47 ± 0.06	0.33 ± 0.03	0.46 ± 0.04	−0.30 ± 0.12
J062355.8–695016.8	06 23 55.83	−69 50 16.8	0.95 ± 0.07	0.69 ± 0.05	0.67 ± 0.03	0.67 ± 0.06	−0.14 ± 0.05

Downloaded from https://academic.oup.com/mnras/article/512/1/265/6522201 by UNI CATANIA FAC AGRARIA user on 27 February 2025

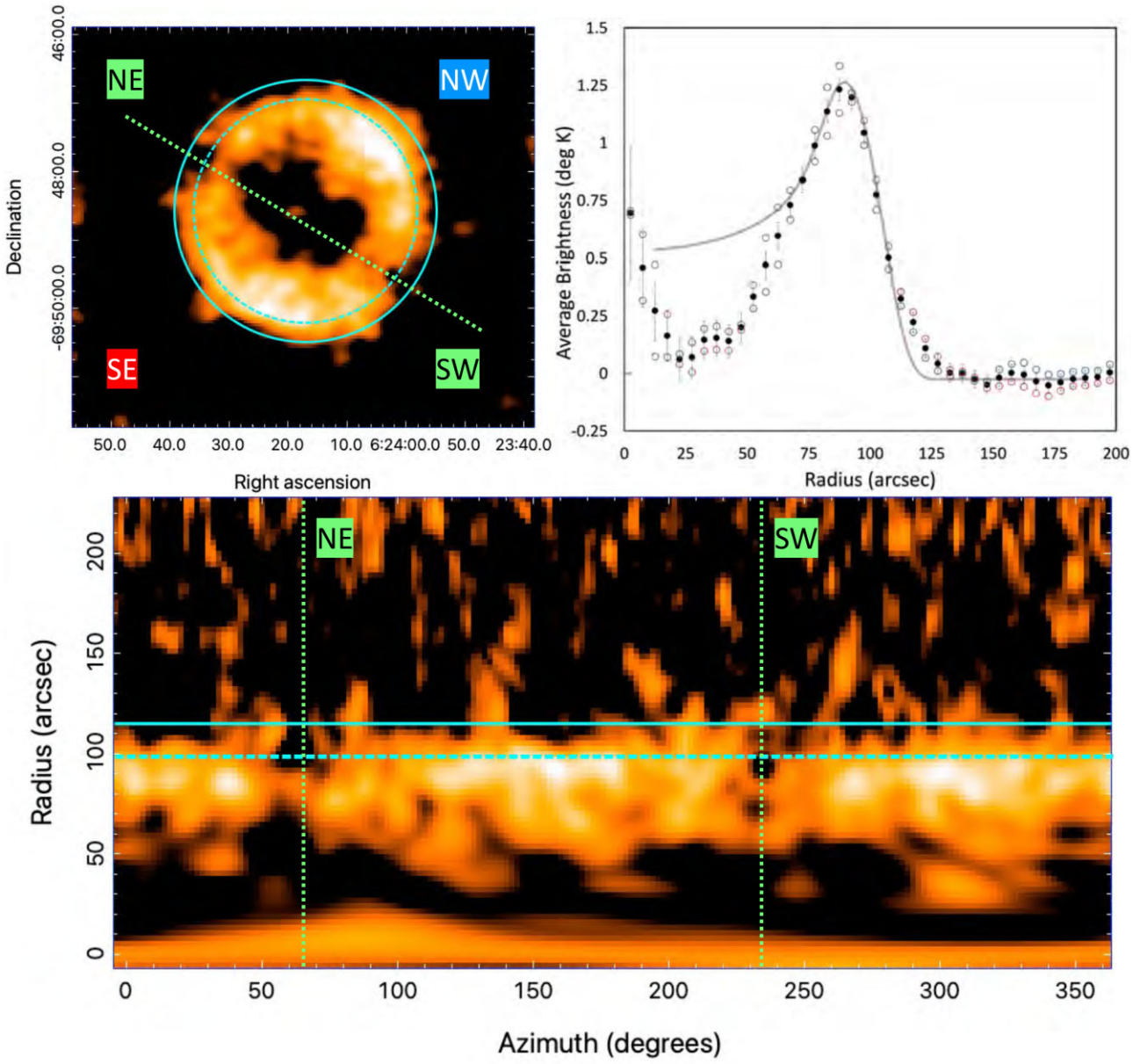

Figure 4. *Top left:* map emphasizing diffuse emission from the J0624–6948, which was made by combining images at 15 and 35 arcsec as described in the text. The dotted green line divides J0624–6948 into two halves. *Top right:* a radial profile plot of J0624–6948, from the effective 10-cm map is shown for the SE (red), NW (blue) halves, and the total (black). Errors represent the error in the mean brightness of each total ring, based on the image rms and the number of independent beam samples in each ring. The errors for the SE and NW halves are not shown, but are $\sqrt{2}$ higher than the corresponding total ring errors. An approximate fit to the peak in the total ring brightness is shown as a (black) solid line; it represents a uniform emissivity shell with a radius of 98 arcsec and width of 10 arcsec, which is seen as 30 arcsec wide in projection. Formal fitting is not possible because the model fails to accurately represent the central brightness. *Bottom:* the effective 10-cm map at 15 arcsec resolution, seen in polar projection (top left image). The angle on the horizontal axis is azimuth from north (0 degrees) through east. The dashed horizontal cyan line, at 98 arcsec, is best-fitting for the radius of the shell in space, prior to projection, for the total ring (black points in the top right graph). The solid horizontal cyan line, at 115 arcsec, is where the diffuse emission cuts off. The best fit has a width (projected width) of 10 arcsec (30 arcsec), so the inner radius of the shell is 93 arcsec.

The most reliable results we expect to get from TT-plots are between frequencies with the largest frequency gap: 888 and 5500 MHz (see Fig. 7), 888 and 9000 MHz, and 2322 and 9000 MHz. We fitted the TT-plots with a linear function of the form: $a + b \cdot T_b$, with a as a free parameter (red in Fig. 7) and with $a = 0$ (green in Fig. 7). The negative y-offset of the red fit is obvious and indicates missing short spacings at the higher frequency. If we now imagine the missing short spacings as a diffuse low surface brightness source that peaks in the centre of J0624–6948, this would change the gradient of the radial profile so that the resulting red fit would be steeper and green fit would be flatter. But since we do not know the amplitude of the missing short spacings, the real spectral index could be anywhere in between. Averaging those fits for the three largest frequency gaps result in a spectral index of $\alpha = -0.4 \pm 0.1$. Since we do not know the proper probability distribution for the spectral index between the two fits, the uncertainty is just a crude estimate. This result is somewhat flatter than the above spectral index estimate of $\alpha = -0.54 \pm 0.08$ but still overlapping.

Downloaded from https://academic.oup.com/mnras/article/512/1/265/6522201 by UNI CATANIA FAC AGRARIA user on 27 February 2025

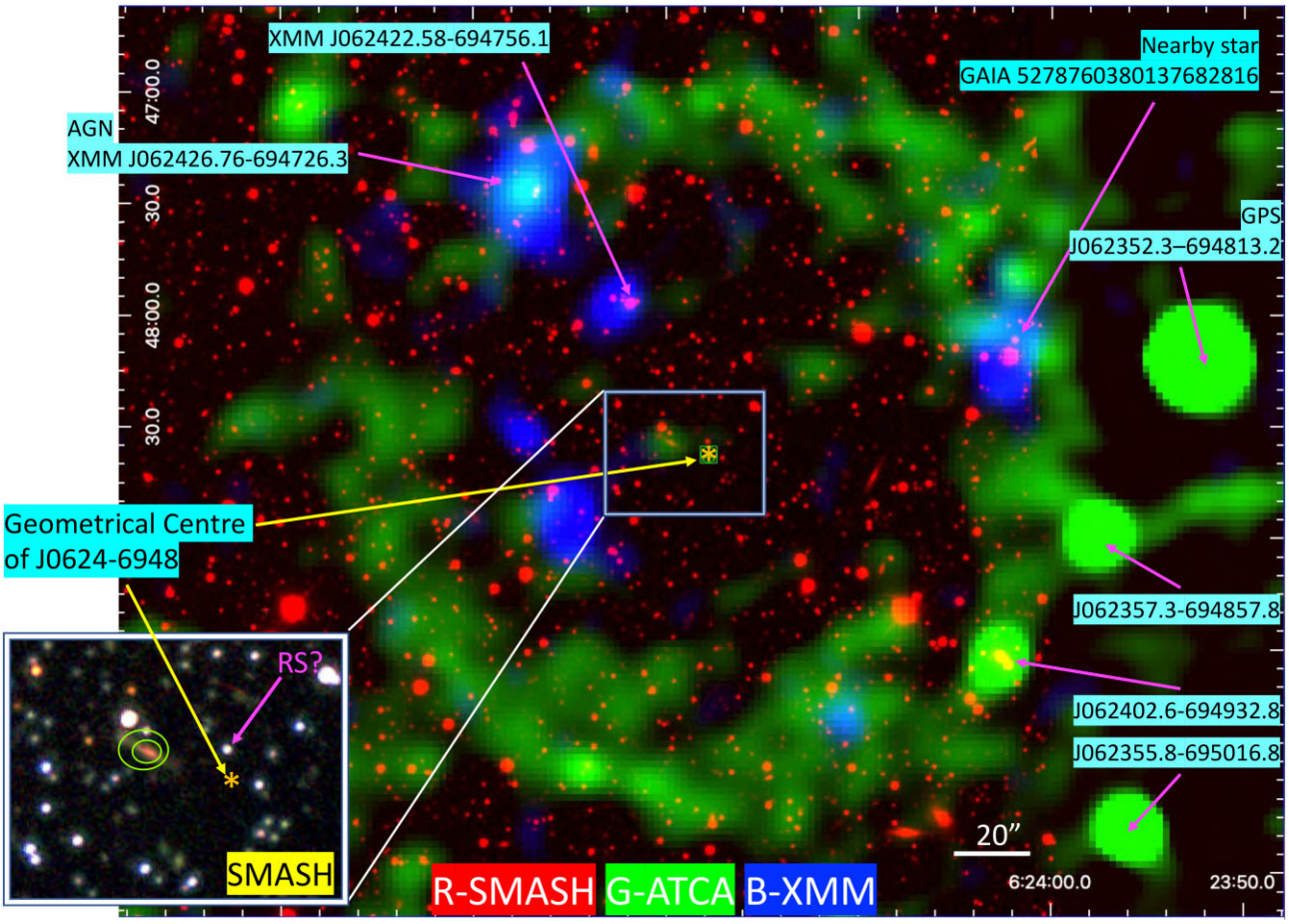

Figure 5. J0624–6948 RGB image (R-SMASH (*i*-band), G-ATCA at 5500 MHz, and B-*XMM-Newton* (0.3–10 keV) indicating the positions of all relevant objects in the field. The inset RGB image at the bottom left is from SMASH where we used bands R (*r*-band), G (*g*-band), and B (*i*-band). The green ellipses are contours from the ATCA 5500 MHz image at 15 and 25 μJy beam^{-1}. At the centre of these ellipses lies a lenticular galaxy ($r = 22.38$ mag) that is located 10.8 arcsec from the J0624–6948 centre. A possible remnant star (RS) from a type Ia SD explosion is indicated by the pink arrow (see Section 4.1.2).

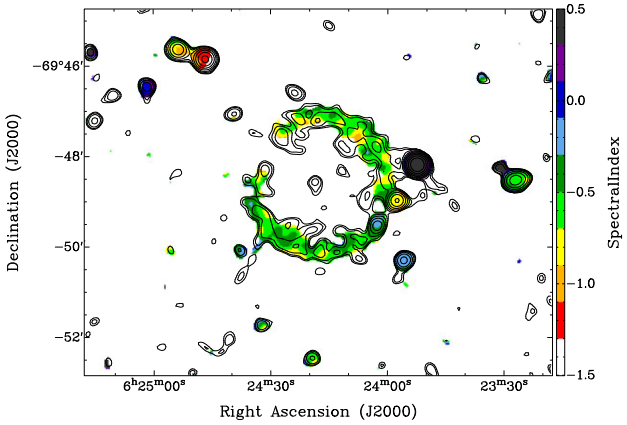

Figure 6. Spectral index map of the LMC ORC J0624-6948 made from ASKAP (888 MHz) and ATCA (2232, 5500, and 9000 MHz) images. Overlaid contours (black) are from ATCA at 2232 MHz and correspond to 0.06 (3σ), 0.105, 0.165, 0.285, 0.525, 1.01, 1.97, and 3.89 mJy beam^{-1}.

3.2 Morphology

The very high degree of circularity of J0624–6948 (compared to the SNR sample of Ranasinghe & Leahy (2019), Lopez et al. (2011)) is evident in the polar projection of the effective 10-cm map (Fig. 4; bottom). The peak brightness of the ring occurs at an approximate sky-projected radius of 90 arcsec. To explore the 2D geometry of J0624–6948, we have created radial profile plots of the NW and SE halves and the total ring. Attempts to model the total J0624–6948 ring profile as the projection of a spherical shell with uniform emissivity over-predict the brightness towards the centre of J0624–6948. This implies that the front and back of the shell have lower emissivities than the sides. Despite the use of a wide range of interferometer arrays (where the shortest baseline is 46-m (array: EW367) at all ATCA frequencies), the missing short spacing problem, already indicated in the discussion about the TT-plots (Section 3.1), is causing a significant reduction of the diffuse emission coming from the shells moving towards us and away from us so that the central region, in particular at the higher frequencies, is nearly devoid of emission.

Because of the missing short spacing problem, our fitting of J0624–6948 with a uniform emissivity shell is only illustrative, giving its approximate radius and width. The radial profiles of the NW and SE halves have slightly different shapes, while the best match for the total ring is a shell of 2D radius 98 arcsec and a width of ∼10 arcsec. A sharp outer edge is visible when looking at the large-scale emission alone; it cuts off at ∼115 arcsec at all azimuths. The 98 and 115 arcsec fiducial radii are shown in Fig. 4 (top right). For all analyses in this

Downloaded from https://academic.oup.com/mnras/article/512/1/265/6522201 by UNI CATANIA FAC AGRARIA user on 27 February 2025

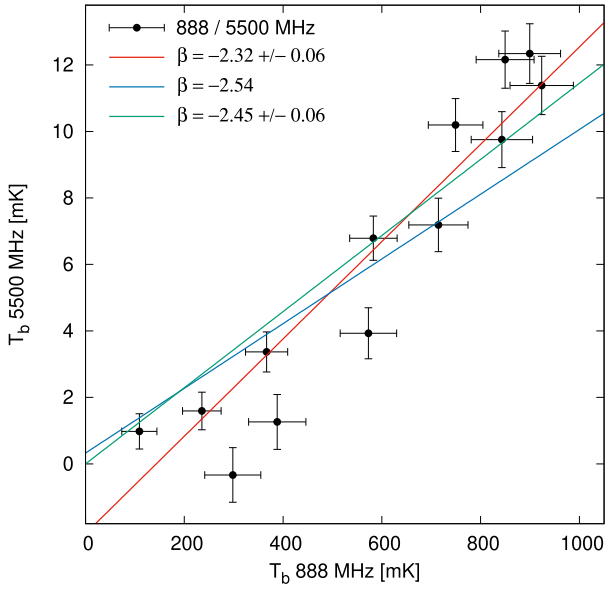

Figure 7. Sample TT-plot between the ASKAP observation at 888 MHz and the ATCA observation at 5500 MHz. The TT-plot is produced from ring-averaged radial profiles that cover the visible shell between 51 and 123 arcsec radius with a 6 arcsec ring separation. The temperature fitted spectrum (β) is indicated in red (with free y-intercept) and green (forcing the linear fit to go through the origin of the diagram) and the blue line indicates a spectrum with a spectral index of −2.54 for comparison (note that $\beta = \alpha + 2$; where α is previously defined flux density spectral index). The fitted red spectrum shows an obvious negative offset from the origin of the diagram for the higher frequency, indicating significant missing short spacings.

paper, we adopt a diameter of 196 arcsec and a shell thickness of 10 arcsec with an error of 4 arcsec.

3.3 Polarization

We searched for polarization from J0624–6948 using the good sensitivity 2232 and 5500 MHz ATCA maps by averaging the total and bias-corrected polarized intensities in concentric rings. We detected no significant polarization at any radius, and determined 3σ upper limits at the location of the peak flux of the ring of 7 per cent and 9 per cent, respectively. There is a marginal (2σ) hint of polarized flux at one location on the 2232 MHz ring, which would need to be verified at higher sensitivity. The only high significance polarization that we detected is associated with the GPS source J062352.3–694813.2 (Fig. 8 and Table 2). While at 2232 MHz, this source is depolarized, at 5500 and 9000 MHz we measure mean polarization fractions of 1.8 ± 0.3 per cent and 2.1 ± 0.2 per cent, respectively.

3.4 X-rays

As there is no obvious X-ray emission that correlates with the extended radio emission from J0624–6948, we run the source detection in the 0.3–10 keV data of MOS1 and MOS2 simultaneously (for the details of the source detection procedure adopted here, see Ducci et al. 2014). We detect five X-ray point sources within the outer circle of J0624–6948, as shown in Table 3. The detection likelihoods for the faintest and brightest sources are ∼23.4 and ∼718.2, respectively. The brightest *XMM-Newton* source in the field, XMMU J062426.76–694726.3 (0.3–10 keV rate, $1.46 \pm 0.08 \times 10^{-2}$ cts s^{-1}, 1σ positional error: $\sigma_{\rm pos} = 0.34$ arcsec) is detected at various infrared WIFES and SMASH optical bands – indicating its 30Dor nature (see Fig. 5). Source XMMU J062402.35 − 694811.1 ($\sigma_{\rm pos} = 0.66$ arcsec) can be associated with the star *Gaia*[1] EDR3 (early data release 3) 5278760380137682816 (see Section 5.2). Sources XMMU J062424.84 − 694853.3 ($\sigma_{\rm pos} = 0.85$ arcsec) and XMMU J062410.68 − 694947.2 ($\sigma_{\rm pos} = 1.10$ arcsec) can be associated with infrared unWISE (Schlafly, Meisner & Green 2019) and CatWISE (Marocco et al. 2021) sources, although the position offsets of the counterparts associated to the *XMM-Newton* sources are large: ∼2.2 and ∼1.8 arcsec for XMMU J062424.84 − 694853.3 and XMMU J062410.68 − 694947.2, respectively. Source XMMU J062422.58 − 694756.1 ($\sigma_{\rm pos} = 0.89$ arcsec) can be associated to the star *Gaia*-EDR3 5278760448849205888 source at a distance of 317 pc (see Fig. 5).

To determine the upper limit of the X-ray flux, we extracted spectra from the area covered by J0624–6948 and from nearby background regions from both the MOS1 and MOS2 vignetting-corrected event lists, produced using the SAS task *evigweight*. The J0624–6948 extraction region was defined based on the centre and dimensions determined above. The J0624–6948 spectra comprise the non-X-ray background (NXB), the astrophysical X-ray background (AXB), and any possible contribution from J0624–6948 itself. The method adopted for constraining the NXB and AXB are described in detail in, e.g. Maggi et al. (2016), Kavanagh et al. (2016), and references therein, whereby the background spectra and filter-wheel closed data are used to constrain the AXB and the NXB, respectively. We account for possible emission from J0624–6948 using a simple collisional ionization equilibrium model. While this model is not formally required, including it in our fits allowed us to determine an upper limit to its contribution. This derived upper limit depends on the shape of the spectrum adopted, i.e. the assumed spectral parameters. Since J0624–6948 is likely an SNR in the ejecta-dominated (ED) or early Sedov phase, (with age estimates in the range from 2200 to 7100 yr, see Section 4.5), we approximated its spectrum as a thermal plasma with a temperature of 1 keV. We then fitted all spectra simultaneously in XSPEC (Arnaud 1996) v12.11.1 using the abundance table of Wilms, Allen & McCray (2000), the photoelectric absorption cross-sections of Balucinska-Church & McCammon (1992), and atomic data from ATOMDB 3.0.9 (http://www.atomdb.org/index.php). We determined the upper limit to the absorbed X-ray flux in the 0.3–10 keV range from the J0624–6948 model normalization upper limit to be 1.2×10^{-14} erg cm^{-2} s^{-1}, corresponding to a surface brightness of 2.4×10^{-15} erg cm^{-2} s^{-1} arcmin^2 over the area of J0624–6948. Assuming the SNR J0624–6948 is more evolved with a temperature of 0.5 keV leads to a minor decrease in these upper limit estimates. If it is less evolved with a temperature of 2 keV, the estimated limits increase by a factor of ∼2.

4 J0624–6948 AS A ROGUE SNR

The overall appearance and radio spectral properties of J0624–6948 suggest a possible SNR origin; if it were found at low galactic latitudes, it would likely be included in existing SNR catalogues. However, its location far from the plane of the MW and from the LMC create challenges for the SNR hypothesis. In this section, we examine the plausibility that J0624–6948 is a rogue SNR associated

[1]The Global Astrometric Interferometer for Astrophysics (*Gaia*) is an European Space Agency (ESA) mission designed to chart a 3D map of Galaxy, providing key positional and radial velocity measurement data (Gaia Collaboration 2021).

Downloaded from https://academic.oup.com/mnras/article/512/1/265/6522201 by UNI CATANIA FAC AGRARIA user on 27 February 2025

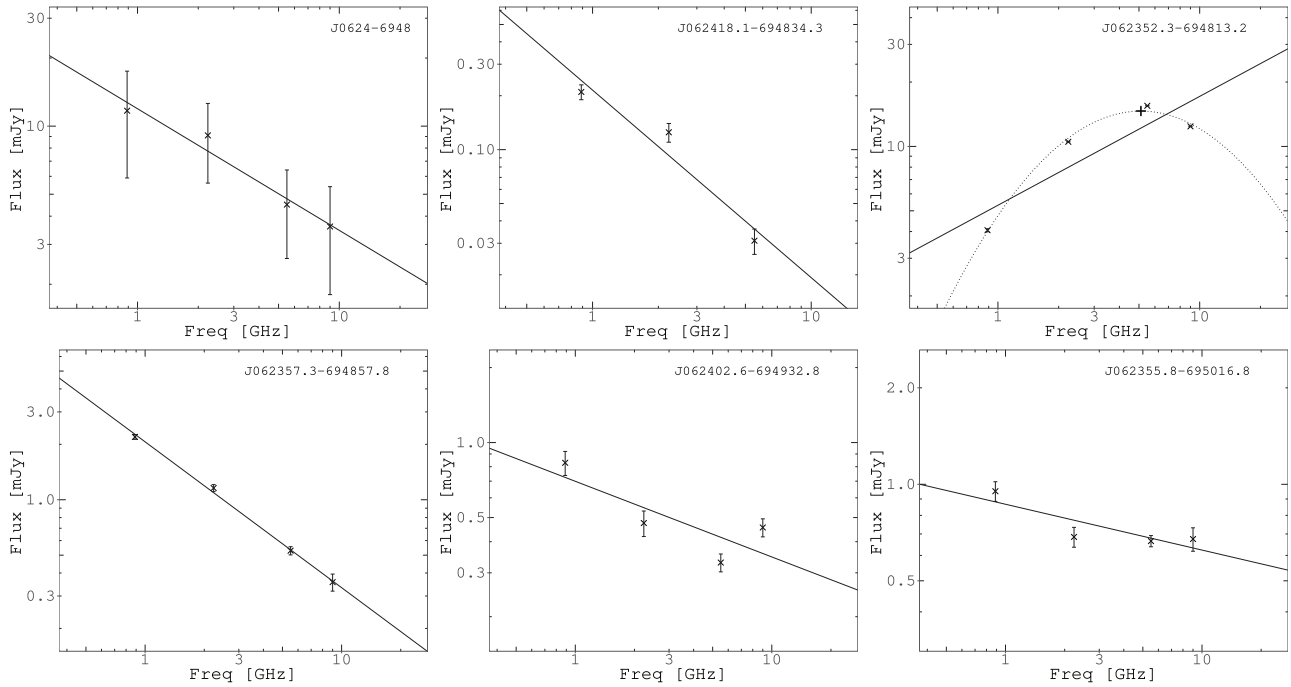

Figure 8. Spectral index plots for J0624–6948 (top left), central source (top middle), and four bright sources near south-west from J0624–6948. See Table 2 for more details. The plus (+) sign in the top right image indicates the turnover frequency at ∼4900 MHz for the GPS source ASKAP J062352.3–694813.2.

Table 3. Details of five bright *XMM-Newton* X-ray sources (0.3–10 keV) near J0624–6948.

Source Name XMMU J	RA (J2000) (degree)	Dec. (J2000) (degree)	σ_{pos} (arcsec)	Likelihood	Count Rate (10^{-2} cts s^{-1})
062426.76–694726.3	96.11223	−69.79074	0.34	748.2	1.46 ± 0.08
062402.35–694811.1	96.00978	−69.80310	0.66	295.3	0.72 ± 0.06
062424.84–694853.3	96.10350	−69.81481	0.85	107.7	0.50 ± 0.06
062422.58–694756.1	96.09409	−69.79893	0.89	46.6	0.28 ± 0.04
062410.68–694947.2	96.04451	−69.82978	1.10	23.4	0.22 ± 0.04

with either the MW or LMC. Because this rogue SNR hypothesis appears quite speculative, we provide a comprehensive look at all the various issues we considered in its evaluation.

J0624–6948 could have either be formed well outside the MW or the LMC bar, or its location could be the result of an explosive kick from an evolved star [post-main sequence (MS)] that began in either galaxy and resulted as an SNR. We thus start with examining possible progenitors in Section 4.1, followed by a summary of what is known about the presumed local environment in Section 4.2. We then look at the radio properties (Section 4.3) and X-ray limits (Section 4.4) to establish whether these are consistent with an SNR origin (Section 4.5).

4.1 Possible progenitors

The uniqueness of the possible SN progenitor may indicate the nature and evolutionary stage of J0624–6948. Here, we examine various scenarios that are based on the object's shape, size, location, and radio properties, as well as the fact that we do not see an obvious counterpart in any other waveband. In Section 3.1, we concluded that there is no associated object such as a pulsar or a PWN in the centre as the nearest pulsar/PWN J0540–69.3 (Brantseg et al. 2014) is more than 4 degrees away. Given the circular shape (Lopez et al. 2011; Ranasinghe & Leahy 2019) and location well outside the MW bar (Hakobyan et al. 2017), J0624–6948 would be more likely a type Ia SN explosion from a star that was formed (and lived) in the outskirts of the LMC. Somewhat less favourably, SN of either type Ia or core-collapse progenitor that came from the LMC as a hypervelocity star (HVS) which travelled across the LMC boundaries and exploded as an SN could also be the origin for J0624–6948.

4.1.1 Hypervelocity runaway from the LMC or MW

Boubert et al. (2017), Boubert, Erkal & Gualandris (2020), and Eldridge, Langer & Tout (2011) suggest that objects like J0624–6948 could result as the remnant of a SN hypervelocity runaway from the LMC or a MW. Evans et al. (2021) notes that the LMC HVSs will outnumber MW ones by a factor ∼2.5.

So-called hostless core-collapse SNe (CCSNe; beyond 10 kpc of the galaxy outskirts) are most likely to come from HVS (Zinn et al. 2011). Direct evidence for the existence of HVS in the LG is shown in Platais et al. (2018) who found 10 LMC runaways over a wide range of masses that appear to have been ejected from the massive LMC star cluster R136 in the tangential plane to distances of up to 98 pc but at only $\upsilon_{max} = 120$ km s^{-1}. Even more convincingly, Edelmann et al. (2005), Przybilla et al. (2008), Irrgang, Kreuzer & Heber (2018), and Erkal et al. (2019) detected the B-star HE 0437–5439 (a.k.a. HVS 3)

Downloaded from https://academic.oup.com/mnras/article/512/1/265/6522201 by UNI CATANIA FAC AGRARIA user on 27 February 2025

as a hypervelocity ($\upsilon = 723$ km s^{-1}) runaway with 9.1 M$_\odot$, which travelled ∼18 kpc from the LMC centre in 20 Myrs. In fact, most observed HVS escaping galaxies are O- and B-type stars (Brown 2015). All these examples suggest that J0624–6948 (if an SNR of CCSNe type) could have a HVS progenitor.

Another possibility is a type Ia progenitor. Such an explosion would occur with a delay after binary formation of $t_{\rm delay} = 300 \times t_{300}$ Myr, where t_{300} is the delay time (the interval between the progenitor formation and the SN type Ia explosion, close to the lifetime of a 3 M$_\odot$ star) in units of 300 Myr (Maoz & Mannucci 2012; Freundlich & Maoz 2021). If the progenitor velocity is zero before formation and constant after formation, the progenitor lifetime is equal to the travel time. If the progenitor is from the LMC then its velocity is $\sim 7/t_{300}$ km s^{-1}. If it is from the Galaxy its velocity is $\sim 160/t_{300}$ km s^{-1}. The lower velocities required for an LMC origin are easier to obtain, thus arguing for that case. However, individual cases could have quite different delay times depending predominantly on the masses and separation of binary components at birth.

The typical SN type Ia would result from the merger of a white dwarf (VLSR)s as a double-degenerate (DD; Webbink 1984) or a VLSR and MS/giant star as a single-degenerate (SD; Whelan & Iben 1973). For a DD scenario, it is unlikely to find any RS because the thermonuclear explosion is believed to completely destroy the white dwarf. An exception to this is the dynamically driven, double-detonation DD scenario, which leads to a surviving hyper-velocity VLSR companion (Pakmor et al. 2013; Shen et al. 2018). On the other hand, for the SD scenario we expect to find a MS, red-giant (RG), or subdwarf B star that would produce a surviving helium donor such as the star US708 (Hirsch et al. 2005; Geier et al. 2015), which is the second fastest unbound MW HVS at a current space velocity of 994 km s^{-1} (Neunteufel 2020). Also, nearby (<2 kpc) 'zombie' stars as VLSRs that survived the thermonuclear explosion, as found by Raddi et al. (2019), are considered, as well as a subclass of the above two that are dynamically driven DD double-detonation (D^6) scenarios (Shen et al. 2018). While these example progenitors are all of Galactic origin, we expect that similar scenarios are quite possible to exist in the LMC, as well as in the old stellar disc region.

The above examples would certainly suggest that the progenitor of SNR candidate J0624–6948 could come from a runaway HVS of CCSNe origin or a normal velocity type Ia progenitor from either galaxy, albeit, with roughly 20 times higher velocities required for MW origin than for LMC origin. For a single star system (CCSNe), massive star lifetimes (10 M$_\odot$ and up) are 25 Myr down to ∼5 Myr (versus delay times for type Ia, which are ∼100 Myr to ∼1 Gyr). Therefore, the peculiar velocities for an origin in the LMC are υ ∼80 km s^{-1} to υ ∼400 km s^{-1} for CCSNe and υ ∼2 km s^{-1} to υ ∼20 km s^{-1} for type Ia. For an origin in the MW, the velocities are much higher: υ ∼2000 km s^{-1} to υ ∼10 000 km s^{-1} for CCSNe and υ ∼50 km s^{-1} to υ ∼500 km s^{-1} for type Ia. However, the location of J0624–6948 on the orbit path of the LMC (see e.g. fig. 6 of Boubert et al. 2017) favour more the LMC scenario than a Galactic one.

In the Super Massive Black Hole (SMBH) slingshot ejection scenario (Hills 1988), velocities as high as $\upsilon = 4000$ km s^{-1} are possible for tidally disrupted close binaries (Brown 2015). In that scenario, the star must originate from the centre of our Galaxy. In fact, an A-type star (S5-HVS 1; Galactic coordinates: $l = 337.4361779510168°$ $b = -57.4004150381868°$) at ∼9 kpc distance from the Sun has been found recently, travelling at a υ ∼1700 km s^{-1} (Koposov et al. 2020; Irrgang et al. 2021) and *Gaia* proper motions showed its origin near the Galactic centre. Hence, there is a possibility that the origin of J0624–6948 as an SNR may be a star that would come from the centre of the MW. However, given that only one such star has been found despite intensive searches (and that one is of relatively low mass), we regard the MW origin scenario as very unlikely. Moreover, the direction of the ejection from the SMBH depends on the orbital plane around the SMBH of the incoming stellar binary, which is not random, because those stars are likely injected from discs of stars or stellar clusters near the Galactic centre.

At much more moderate velocities of 70–350 km s^{-1}, a dynamical ejection from a LMC stellar cluster is very plausible (Gualandris & Portegies Zwart 2007). We note that HVS 3 is more than twice as distant from the LMC centre as J0624–6948 and, accordingly the ejection velocity would need to be as high as $\upsilon = 870$ km s^{-1}(Irrgang et al. 2018). This is very hard to achieve in dynamical ejection scenarios unless an intermediate mass stellar black hole is involved (Fragione & Gualandris 2019). The lower ejection velocities that we derived can be explained without invoking exotic mechanisms.

In summary, a variety of HVSs are known in both the LMC and MW, and their properties make them plausible candidates for the progenitor of J0624–6948.

4.1.2 Evolved star from the old LMC stellar disc

We also examine the scenario that the progenitor of SNR candidate J0624–6948 is a star that has always lived in the old (outer) stellar disc of the LMC, but formed more recently. Despite the sparsity of matter in this region, there could be localized new star formation triggered by disequilibrium due to the interactions between the LMC and the stellar and dark matter haloes of the MW.

There is clear observational evidence of local outflows emanating from supergiant shells in the LMC and a trailing filament of H I gas mainly originating from the 30-Doradus region, as well as the Leading Arm connection. Indeed, looking in the Parkes Galactic All-Sky Survey (GASS/HI4PI; angular resolution is ∼16.2 arcmin; HI4PI Collaboration (2016)) H I image (Fig. 9), we can see that the LMC H I envelope covers a much larger area than the optical (and radio-continuum) emission, including the location of this new object that is within the H I envelope of the LMC.

Evidence and modelling for the presence of such interaction waves and star formation has been presented by Besla et al. (2016) and Conroy et al. (2021). SMASH (Nidever et al. 2021), SkyMapper, and the WIFES all-sky Mollweide projection images do show an increased density of K giant stars 60–100 kpc from the Galactic centre, especially in the NE and SW regions (in equatorial sense) of the Galactic Halo (Conroy et al. 2021). The latter may be due to the local wake of the passage of the LMC. The model of Conroy et al. (2021, their fig. 1) predicts some local increased stellar density in our region of interest between the LMC and MW, albeit relatively small. Nevertheless, several recent studies confirm a large envelope of stars around the LMC (and MW; Cullinane et al. 2020). This strongly argues that a range of stellar variety would already exist in these regions for at least the past tens-to-hundreds of million years. We also note that the location of J0624–6948, some 3 degrees from the edge of the LMC bar, is just within the outer shell of stars that surround the LMC, clearly apparent in a large-area WIFES W1 (3.4 μm) panoramic mosaic of the LMC region (Jarrett et al. 2019), which suggests J0624–6948 is still within the outer confines of the LMC dwarf galaxy.

The situation with respect to the MW is a little more complicated. J0624–6948 is located at a Galactic longitude of about 280° at 28° from the Galactic plane. For the evolutionary models discussed below, we adopt a somewhat arbitrary 5 kpc distance for a MW origin. Adopting this distance does cause some problems; at 5 kpc

Downloaded from https://academic.oup.com/mnras/article/512/1/265/6522201 by UNI CATANIA FAC AGRARIA user on 27 February 2025

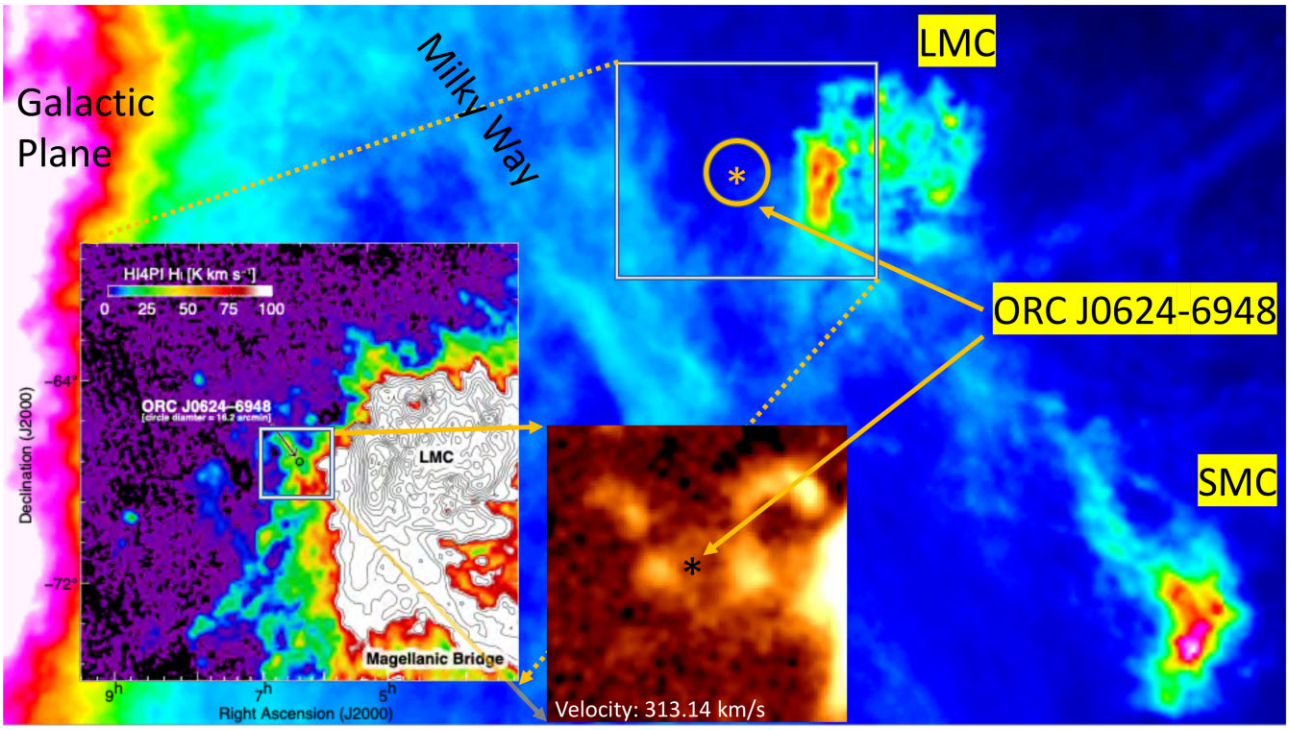

Figure 9. The Parkes GASS and HI4PI (insets) H I images indicating the position of J0624–6948 with respect to the LMC, SMC, and MW. The image beam size is 16.2 arcmin. In the leftmost inset, the integrated velocity range is from υ=189.5 to υ = 319.6 km s^{-1}. The contour levels are 100, 150, 250, 400, 600, 850, 1150, 1500, 1900, 2350, and 2800 K km s^{-1}.

distance it would be about 2.5 kpc below the Galactic plane, away from any potential formation site within the MW for its progenitor star. However, if J0624–6948 were much closer, it would be very small in linear size and very young, so the SN should have appeared in the historical record (see Appendix A). Further away than 5 kpc would increase the distance from the plane and make a relation to the MW even less likely. We could, of course, find the location of the spiral arms in the plane of the Galaxy and optimize the potential distance to J0624–6948 within the MW, but that is not constrained by our data so we adopt an optimal distance of 5 kpc, if J0624–6948 is related to our Galaxy.

We queried the SMASH public data release 2 (Nidever et al. 2021), which covers the region surrounding J0624–6948, and in Fig. 10 display a colour-magnitude diagram (CMD) showing all stars with robust photometry within 12 arcmin of its geometric centre to sample the local stellar population. LMC members are clearly the dominant population at this location, providing weak statistical evidence that J0624–6948 is indeed associated with the LMC under the assumption that it has a stellar origin. Isochrones from the MIST library (Choi et al. 2016; Dotter 2016) suggest that most stars in the vicinity of J0624–6948 have ages older than ∼1 Gyr, but there are also low-density younger populations present with ages down to ∼200 Myr. However, when considering stars projected within the ring itself (i.e. within a radius of 100 arcsec of its geometric centre), there are no objects obviously younger than ∼1 Gyr. Overall, this indicates that the type of stellar populations expected to host a type Ia SN are abundant at this location, while the young massive stars required for a SN CC are exceedingly rare.

There are four stars within 20 arcsec of the centre of J0624–6948 that have evolved off the MS. These are marked with yellow points in Fig. 10. The most interesting of these is a star on the lower red giant branch, which sits just <4 arcsec from the centre of J0624–6948 (see Fig. 5 left inset) and, according to the stellar tracks, must be at least ∼4 Gyr old. This is a plausible candidate for a surviving companion (RS) from a SN type Ia SD scenario, but is too faint for *Gaia* EDR3 to provide any astrometric data.

There are recent discoveries of another two similar objects located in the outskirts of the LMC. Only ∼11 arcmin (or 160 pc at the distance of the LMC) east from J0624–6948 is the LMC classical nova AT 2018bej (Chomiuk et al. 2018; Ducci et al. 2020). While also possible, we have no evidence that AT 2018bej resulted from a runaway star. This nearby location of a similar type of object further strengthens an LMC SNR scenario. A second possible runaway (or isolated) SNR candidate (LMC SNR J0509-6402) is detected in a recent optical study by Yew et al. (2021) and is positioned some 2° (1.75 kpc) north from the outermost (radio-continuum) boundaries of the LMC but well inside of the LMC H I envelope. While this LMC SNR candidate is a bit larger (D = 107 pc), the most distinctive difference to J0624–6948 is the lack of radio detection.

Several Galactic SNRs are detected at high Galactic latitudes but none is seen at distances further than a few kpc (Vukotić et al. 2019). Another two high-latitude Galactic SNRs are detected in new *eROSITA* X-ray images (Becker et al. 2021; Churazov et al. 2021) and are associated with the MW but at distances of up to ∼3 kpc. These two are older (40 kyr) Galactic SNRs and tentatively classified as Type Ia SN explosions. However, none of these sources have a strong radio-continuum signature, which is different from J0624–6948 and further challenges our understanding of the physical processes that would occur in such objects.

4.2 The local environment: MW and LMC alternatives

If J0624–6948 is associated with the LMC, then, with a nominal distance of 50 kpc, it would be 2.5–3 kpc away from any potential

Downloaded from https://academic.oup.com/mnras/article/512/1/265/6522201 by UNI CATANIA FAC AGRARIA user on 27 February 2025

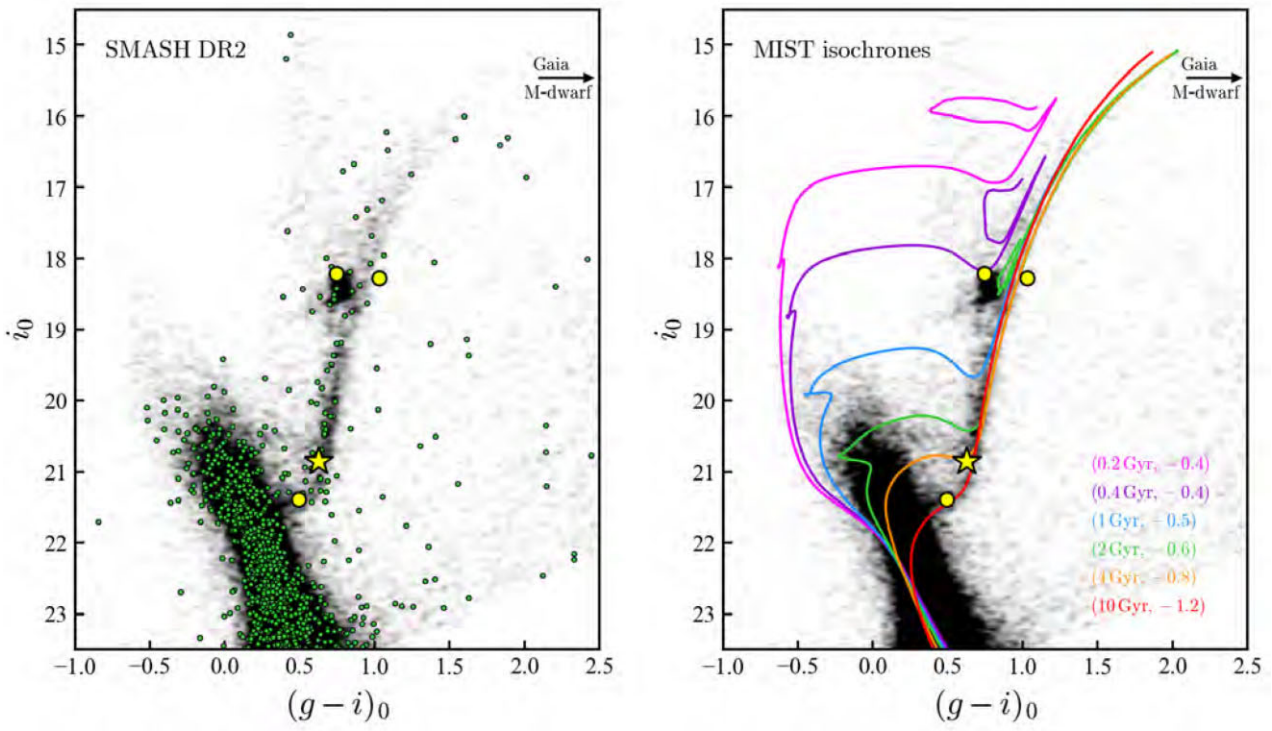

Figure 10. CMDs for stars in the vicinity of J0624–6948 from SMASH DR2. *Left:* stars within 12 arcmin of the geometric centre of J0624–6948 indicate the typical local populations and are plotted in grey as a smoothed Hess diagram (projected density distribution). Stars projected inside the ring itself (i.e. located within 100 arcsec of its centre) are marked by green points, and the four evolved stars within 20 arcsec by yellow points. The star on the lower part of the RGB discussed in the text (also see left inset in Fig. 5) is marked with a star symbol. The arrow to the upper right indicates the location of the *Gaia* M-dwarf discussed in the text, which has colour $(g-i)_0 = 3.24$. *Right:* Isochrones from the MIST library (Choi et al. 2016; Dotter 2016) over-plotted on the same Hess diagram as shown in the left-hand panel. These are appropriate for the observed age–metallicity relationship in the LMC field (e.g. Piatti & Geisler 2013). For clarity, evolution after the helium flash is shown only for the 200 Myr, 400 Myr, and 2 Gyr isochrones; the loci for the 1, 4, and 10 Gyr tracks are very similar to that of the 2 Gyr isochrone.

progenitor formation site. Similarly, we argued in Section 4.1.2 that the most plausible distance from the Galactic Plane is 5 kpc. We have shown above that this is plausible in both the hypervelocity and old, outer disc scenarios. The LMC 50 kpc distance is well-constrained, since even a distance of 45 or 55 kpc, e.g. would place J0624–6948 at an implausibly large 5–6 kpc away from the LMC. Therefore, in the absence of good constraining data, we adopt a distance of 50 kpc for J0624–6948 assuming it is related to the LMC.

The only direct information on the local environment comes from H I observations, but only when averaged over large scales, which may or not reflect the immediate environment of the presumed SNR. The integrated intensity of H I in the vicinity of J0624–6948 is ∼25 K km s^{-1} (over the velocity range υ ∼190 km s^{-1} to υ ∼320 km s^{-1}, corresponding to the LMC component; see inset, Fig. 9). This corresponds to a column density $N_{\rm H}$ of ∼4.5 × 10^{19} cm^{-2}. At the location of the J0624–6948, this cloud is ∼1 degree wide, which would translate to ∼0.9 kpc at the assumed LMC distance of 50 kpc. If we assume that the H I is distributed evenly along a 0.9 kpc line of sight, we can get an approximation of the average ambient density of the SNR. Dickey & Lockman (1990) determined that H I column densities derived assuming optically thin emission should be multiplied by 1.1–1.3 to account for H I self-absorption. Using 1.2 as a medium value, we get an integrated H I column density of 5.4 × 10^{19} cm^{-2}. Another factor of 1.1 gives an atomic column density of 6 × 10^{19} cm^{-2}, taking the Helium into account. With the line of sight of 0.9 kpc, we find an average density of 0.017 cm^{-3}.

4.3 Properties of J0624–6948 as an SNR candidate

In this section, we assume that there is a plausible SN progenitor, as discussed above. We then provide a comprehensive examination of the observed radio properties and X-ray limits of J0624–6948 to evaluate the plausibility that it is an SNR.

4.3.1 Size, structure, and radio spectrum

The circular appearance of J0624–6948 and the prominence of its radio emission compared to other wavelengths are consistent with the SNR hypothesis. With the above determined potential distances, J0624–6948 would have a radius of about $R_{\rm LMC} = 23.8$ pc if it is related to the LMC and a maximum of $R_{\rm MW} = 2.4$ pc if related to the MW. Both of these are plausible. In addition, J0624–6948's bilateral symmetry, along the NW–SE axis (Fig. 4; top left)[2], makes it similar to nearly 45 per cent of shell-type Galactic SNRs (West et al. 2016).

We note that the J0624–6948 extreme circularity (see Section 3.2) is unusual for a SNR; we can find only a handful of similar examples, such as the young (under 2000 yr old) MCs SNRs, such as SN1987A (Cendes et al. 2018), MC SNR J0509–6731 (Bozzetto et al. 2014; Roper et al. 2018), and N 103B (Alsaberi et al. 2019). This high level

[2]A shell-type SNR with two lobes of emission, separated by a symmetry axis (West, Safi-Harb & Ferrand 2017); also called 'barrel shape'.

Downloaded from https://academic.oup.com/mnras/article/512/1/265/6522201 by UNI CATANIA FAC AGRARIA user on 27 February 2025

of circularity in J0624–6948 might be the result of an explosion in a uniform and low-density environment.

The spectral index of $\alpha = -0.4 \pm 0.1$ (see Section 3.1) is somewhat flatter than that of the average shell type SNR but within the observed range of –0.55 ± 0.20. (Reynolds et al. 2012; Galvin & Filipović 2014; Bozzetto et al. 2017; Maggi et al. 2019; Filipović & Tothill 2021a). For example, we note another relatively young shell-type SNR at high latitude is the SNR G182.4 + 4.3 discovered by Kothes, Furst & Reich (1998) with a similar radio spectral index of $\alpha = -0.42$.

SNRs are also characterized by their position in the brightness–to–diameter (Σ–D) parameter space. With $S_{1\,\mathrm{GHz}} = 11.3$ mJy, assuming that the ASKAP observations at 888 MHz include all required angular scales and $\alpha = -0.4$, we estimate a radio surface brightness at 1 GHz of $\Sigma = 1.6 \times 10^{-22}$ W m^{-2} Hz^{-1} sr^{-1} (assuming the emission to be spread smoothly over a circle of 196 arcsec diameter). This value would place J0624–6948 in the bottom area of the SNR Σ–D diagram (Pavlović et al. 2018; Urošević 2020, their fig. 3). If it is located in the MW, J0624–6948 would be positioned in the lower left corner of the Σ–D diagram in Pavlović et al. (2018, their fig. 3) and Urošević (2020), indicating free expansion and an unrealistic low-ambient density. For an LMC location, it would be positioned in the lower right corner, indicating a Sedov phase SNR with still very low-ambient density. While the low radio surface brightness clearly points to an LMC location, we note that the transitional phase may last even longer than the well-defined free expansion or Sedov phases (Petruk et al. 2021). Finally, as pointed by Pavlović et al. (2018), the radio brightness in free expansion phase is expected to rise with time as we can also observe in the youngest Galactic SNR G1.9 + 0.3 (Luken et al. 2020). But if SNR is in transition or Sedov phase, its brightness first plateau and then starts decreasing. This might be a good future indicator for the J0624–6948 evolutionary stage where the next generation of radio observations might help solving this question.

We looked for further clues to the nature of J0624–6948 from its bilateral appearance (Fig. 4). The bilateral morphology of J0624–6948 resembles a number of well-known high-latitude MW SNRs, such as SN 1006 (Reynoso, Hughes & Moffett 2013), G296.5 + 10.0 (Harvey-Smith et al. 2010), G119.5 + 10.2 (Sun et al. 2011), and G93.3 + 6.9 (Kothes et al. 2006), as well as young ones like G1.9 + 0.3 (De Horta et al. 2014; Luken et al. 2020). A number of studies have looked at the difference angle between the symmetry axis, e.g. and the position angle of the plane of the MW. At low latitudes, the symmetry axis is broadly parallel to the MW plane (Gaensler 1998; West et al. 2016), with exceptions occurring at high Galactic latitudes, where they tend to be perpendicular (West et al. 2016). J0624–6948's symmetry axis is at position angle of 60(240) degrees (measured in equatorial coordinates), while lines of constant Galactic latitude have position angles of –4(176) degrees, so no special relationship is seen. On the other hand, the orientation of the LMC bar is 66(246) degrees, which is quite close to the J0624–6948 value.

Large-scale magnetic fields in galaxies have geometries that typically follow their spiral arm pattern, and the LMC has a geometry that is closer to face-on than edge-on, with an inclination angle of ∼35 degrees (Nikolaev et al. 2004). We expect that the large-scale magnetic field of the LMC would be weak at the distance of J0624–6948; given this, and the expectation that the magnetic field would follow the spiral pattern, there is no particular reason to expect a relationship between the symmetry axis of J0624–6948 and the orientation of the LMC bar (Filipović et al. 1998). At the present time, there are no studies of the large-scale magnetic field of the LMC that go out that far to verify whether there is a clearer relationship between the orientation of J0624–6948 and the large-scale magnetic field of the LMC. We also note that a number of MCs SNRs – 1E0102–72.3 (Alsaberi et al., in preparation), SXP 1062 (Haberl et al. 2012), and MC SNR J0509–6731 (Bozzetto et al. 2014; Roper et al. 2018) – show bilateral symmetry, but without the clear connection with large-scale galaxy structure.

To some extent, J0624–6948 could be similar (on a smaller scale) to Galactic Radio Loops identified in the MW (Dickinson 2018; West et al. 2021) but at larger distances. One would expect a handful of such SNRs (or (super)bubbles) around the LMC/SMC and several around the MW (Norris et al. 2021b).

4.3.2 Polarization of J0624–6948 as SNR

As shown in Section 3.3, only an upper limit of 7–9 per cent can be placed on the polarization fraction of J0624–6948. Although a detection of polarization on the ring of J0624–6948 would help support an SNR origin, our upper limits mentioned above are still very much consistent with the SNR scenario. Most young SNRs typically are not strongly polarized because of the highly turbulent magnetic field (Anderson, Keohane & Rudnick 1995; Bozzetto et al. 2014; Luken et al. 2020). For example, the MW SNR Cassiopeia A at 5 GHz shows a mean degree of polarization in the diffuse plateau region of ∼8–10 per cent, while the ring fractional polarization drops to ∼5 per cent (Anderson et al. 1995). Another striking example is the historical SNR G11.2–0.3 from A.D. 386. This SNR has only about 2 per cent integrated polarization at 32 GHz, but shows both radial and tangential magnetic fields in its shell, indicating it is transitioning between the free expansion phase and the Sedov–Taylor phase (Kothes & Reich 2001). The low polarization is also true for old SNRs in the radiative phase where the thermal electron population causes depolarization and thus there is a very little polarized emission, at lower frequencies (Filipović & Tothill 2021b). Galactic SNR S147 is a good example of this (Xiao et al. 2008). These older remnants, however, are not a good comparison for J0624–6948, because for these very depolarized cases (like S147), we would also see an optical counterpart, which we do not detect here. And in this case, one would expect to see higher polarized fractions at high frequencies.

At the other extreme, Reynoso et al. (2013) found in the case of the young SNR SN1006 or G327.6 + 14.6 [radius ∼10 pc and expanding in a denser environment (∼0.05 cm^{-3}; Acero, Ballet & Decourchelle 2007)] than the ISM around J0624–6948), a mean fractional polarization of 17 per cent. The recently discovered MW SNR G181.1 + 9.5 serves as a nice example of what can happen in a low-density environment, as it shows 70–80 per cent polarization at 5 GHz, and is in the late-Sedov or early-radiative phase (Kothes et al. 2017).

From the lack of polarization and lack of depolarizing optical emission, we suggest that J0624–6948 is most likely a young SNR that is still expanding freely or at least in the early-Sedov phase, in a low-density environment.

4.4 X-ray and local environment constraints

J0624–6948, as an SNR at the distance of the LMC (50 kpc), would have an X-ray luminosity upper limit of $\sim 5 \times 10^{33}$ erg s^{-1} for a temperature of 1 keV and $\sim 9 \times 10^{33}$ erg s^{-1} for a temperature of 2 keV. The lowest luminosity of SNRs in the LMC (from Maggi et al. (2016, 2019), Haberl et al. (2012), and Maitra et al. (2021)) are $\sim 7 \times 10^{33}$ erg s^{-1} so J0624–6948 would be among the faintest

Downloaded from https://academic.oup.com/mnras/article/512/1/265/6522201 by UNI CATANIA FAC AGRARIA user on 27 February 2025

LMC SNRs, assuming it is indeed an SNR and at the distance of the LMC. In addition, these upper limits to the X-ray luminosity are significantly lower than ordinary SNRs of similar radius in the Sedov phase, evolving into densities ∼0.1–1 cm^{-3}, typical of the LMC, which have X-ray luminosities of 10^{34}–10^{36} erg s^{-1} (Maggi et al. 2016).

Given its large degree of circularity, the local density at the location of J0624–6948 at ∼3 kpc from the LMC and ∼50 kpc (Section 4.2) from the Sun is expected to be as low as 10^{-1}–10^{-4} cm^{-3} (Hurley-Walker et al. 2019a,b). As for the MW origin, we expect a similar range of environmental densities.

There are 6 SNRs in Pavlovic et al. (2014) that have radio surface brightness similar to or lower than the estimated surface brightness of J0624–6948 (1.6×10^{-22} W m^{-2} Hz^{-1} sr^{-1} and similarly large diameters. Those are: G65.1+0.6 (1.8/176), G96.0+2.0 (0.67/30.3), G114.3+0.3 (1.7/14.3), G152.4–2.1 (0.56/31.1), G156.2 + 5.7 (0.62/32), and G190.9–2.2 (0.4/18.8), where surface brightness/diameter in parentheses are given in units of 10^{-22} W m^{-2} Hz^{-1} sr^{-1} and pc, respectively. The ambient densities are only known for those with X-ray spectra (Leahy, Ranasinghe & Gelowitz 2020), which includes only G156.2 + 5.7, which has ISM density of 0.20 cm^{-3}. Thus, G156.2+5.7 has comparable radio properties to J0624–6948, but is much brighter in X-rays. For G156.2 + 5.7 to have similar X-ray luminosity to the upper limit of J0624–6948, it would have to have a factor of ∼30 lower ISM density, i.e. 0.007 cm^{-3}.

We do not expect to find strong SNR shock tracers in such a rarefied intergalactic environment as in the future optical ([S II] and/or [O III] emission lines) or in deeper X-ray observations. The intensity of the thermal X-ray emission of hot gas scales as the square of the environmental density. An expansion in a very rarefied environment would be faster. Therefore, the reason for faintness in X-rays is the low density in the shock. And similarly, we do not necessarily expect to detect optical emission because of the low-ISM density. As shown in Yew et al. (2021), optical emission from SNRs generally comes from high-density clouds and filaments overrun by the SN shock.

Finally, an SNR originating from a type Ia explosion would be quite circular despite a peculiar (with respect to the local ISM) progenitor velocity of υ ∼10–100 km s^{-1}; the small ratio of peculiar velocity to the shock velocity, which is expected to be in the 1000's of km s^{-1} and the unperturbed ISM, ensures this. In contrast, any remnant following from a CCSN of a star moving with υ ∼70–350 km s^{-1} would expand into a strongly elongated stellar wind-bubble created by the progenitor's wind. The resulting SNR would be highly non-spherical as shown for instance by Meyer et al. (2015, 2021). We note that the stellar progenitor type is unknown, however, any massive star undergoing significant mass-loss would create a sizeable bubble and give rise to a similar non-spherical structure. This renders a type Ia progenitor scenario more likely than a CCSNR scenario.

4.5 Evolutionary state

The low percentage polarization of the radio continuum emission, which indicates a lot of turbulence and therefore still strong interaction between the SN ejecta and the swept up material, points to an SNR that is either still expanding freely or at least in the early-Sedov phase. In addition, we find a shell width that is about 10 per cent of the SNR's radius, pointing to an adiabatic expansion and therefore again to the Sedov phase. We therefore assume from now on that our potential SNR J0624–6948 is adiabatically expanding and thus in the early-Sedov phase.

We apply the models of McKee & Truelove (1995) to study the possible evolutionary state of J0624–6948 at the two potential locations. As J0624–6948 most likely is in the early-Sedov phase, we use the time t_{st}, the age that marks the transition between free expansion and Sedov phase, as a reference time. According to McKee & Truelove (1995), the well-known young SNRs Cas A, Kepler, and Tycho would all likely be younger than t_{st} and SN 1006 a little older. The radius R_{st} at t_{st} depends only on the ambient density and the ejecta mass M_{ej} of the SN explosion. We assume for a type Ia explosion $M_{ej} = 1.4$ M$_\odot$ and for a CCSNe explosion $M_{ej} = 10$ M$_\odot$. This would result in ambient densities n_0 of ≥1.2 cm^{-3} (type Ia) and ≥8.0 cm^{-3} (CCSNe) for a MW location and $n_0 = 0.001$ cm^{-3} (type Ia) and $n_0 = 0.008$ cm^{-3} (CCSNe) for a LMC location. The low radio surface brightness, the missing thermal X-ray emission, and the location far away from any star-forming environment pretty much negate an environment as dense as required for the MW location.

Using the equation by McKee & Truelove (1995), we determine the age t_{st} of J0624–6948 for the different locations and SN explosions to be 215 yr (type Ia) and 712 yr (CCSNe) for a MW location and 2200 yr (type Ia) and 7100 yr (CCSNe) for a LMC location for an explosion energy of 1.5×10^{51} erg for the type Ia explosions (Khokhlov, Mueller & Hoeflich 1993), and the canonical explosion energy of 10^{51} erg for the CCSNe explosions. Further characteristics of these cases are listed in Table 4.

We used the equations for the hydrodynamic evolution of a young SNR by McKee & Truelove (1995) to estimate SNR characteristics and list them in Table 4. In addition to SNRs that are evolutionary at the transition between ED and Sedov phase, which we already discussed above for the MW and the LMC location, we added cases for type Ia and CCSNe explosions expanding into constant ambient densities estimated above from the upper limit of the X-ray emission ($n_0 = 0.007$ cm^{-3}) and from the H I observations ($n_0 = 0.017$ cm^{-3}). Also, we explore the 'unified SNR evolutionary models' but only for type Ia SN in Appendix A. All of the results we calculate for the LMC location look quite reasonable for our observations.

The low percentage polarization rules out that the swept up material is dominating the expansion. In that case, we would expect quite homogeneous magnetic fields and therefore high percentage polarization, at least at the higher frequencies. From this, we can certainly rule out the somewhat higher ambient density we get from the H I observations and assume an upper ambient density of about 0.005 cm^{-3} for a type Ia explosion. We can get another limit from the low radio surface brightness and the width of the shell that makes up about 10 per cent of the source's radius. This rules out a very early evolutionary phase and gives us a lower limit of about 0.008 cm^{-3} for a type II CCSN. Therefore, based on this, we are not able to definitively say if J0624–6948 was a type Ia or a CCSN explosion.

5 ALTERNATIVE SCENARIOS FOR J0624–6948 ORIGIN

Given the unusual nature of the rogue SN origin presented above, we also explore a variety of alternative explanations for the origin of J0624–6948.

5.1 Odd radio circle

ORCs are circles of faint diffuse radio emission found in large-area surveys (Koribalski et al. 2021; Norris et al. 2021b), which are undetected at other wavelengths. Three of the five known ORCs are single, and each of these has an elliptical galaxy at its centre at a redshift of $z \sim 0.2$–0.5. Each of these host galaxies is located in an

Downloaded from https://academic.oup.com/mnras/article/512/1/265/6522201 by UNI CATANIA FAC AGRARIA user on 27 February 2025

Table 4. J0624–6948 as an SNR at LMC and MW distances and with various ISM densities. Calculation of characteristics are based on McKee & Truelove (1995). We show the distance d, radius r, ejecta mass M_0, explosion energy E_0, ambient density n_0, age t, velocity v_b, and temperature T_b at the blast wave location, and the swept up mass M_{sw}. We used the average explosion energy of 1.5×10^{51} erg observed for extragalactic type Ia SN explosions (Khokhlov et al. 1993). SNII CCSNe typically have explosion energies between 10^{50} and 10^{51} erg (Pejcha & Prieto 2015). We used those lower and upper limits for CCSNe together with a representative ejecta mass of 10 $M_\odot$.

(1) Location (MW/LMC)	(2) d (kpc)	(3) r (pc)	(4) SN type	(5) M_0 ($M_\odot$)	(6) E_0 (10^{51} erg)	(7) n_0 (cm^{-3})	(8) t (yr)	(9) v_b ($km\,s^{-1}$)	(10) T_b 10^7 K	(11) M_{sw} ($M_\odot$)	(12) Comments
MW	5	2.4	SNIa	1.4	1.5	1.2	215	6780	63.8	2.3	$t = t_{st}$ ED/Sedov
MW	5	2.4	CCSNe	10	0.1	8.0	2250	655	0.6	16	$t = t_{st}$ ED/Sedov
MW	5	2.4	CCSNe	10	1.0	8.0	712	2070	6.0	16	$t = t_{st}$ ED/Sedov
LMC	50	23.8	SNIa	1.4	1.5	0.001	2200	6780	63.8	2.3	$t = t_{st}$ ED/Sedov
LMC	50	23.8	CCSNe	10	0.1	0.008	22500	655	0.6	16	$t = t_{st}$ ED/Sedov
LMC	50	23.8	CCSNe	10	1.0	0.008	7100	2070	6.0	16	$t = t_{st}$ ED/Sedov
LMC	50	23.8	SNIa	1.4	1.5	0.007	4000	2600	9.3	12.4	Sedov
LMC	50	23.8	SNIa	1.4	1.5	0.017	5500	1800	4.4	30	Sedov
LMC	50	23.8	SNIa	1.4	0.5	0.007	6510	1600	3.6	12.4	Sedov
LMC	50	23.8	SNIa	1.4	0.5	0.017	9550	1032	1.5	30	Sedov
LMC	50	23.8	CCSNe	10	0.1	0.007	21300	712	0.7	12.4	late ED
LMC	50	23.8	CCSNe	10	1.0	0.007	6740	2250	7.0	12.4	late ED
LMC	50	23.8	CCSNe	10	0.1	0.017	26400	460	0.3	30	early Sedov
LMC	50	23.8	CCSNe	10	1.0	0.017	8350	1450	2.9	30	early Sedov

overdensity or is interacting with a companion (Norris, Crawford & Macgregor 2021a). These single ORCs probably represent a spherical shell of emission caused by a shock wave from the central host galaxy (Norris et al., 2022, in preparation). The remaining two ORCs form a pair, separated by less than 1 arcmin, which may be associated with a nearby double-lobed radio 30Dor (Macgregor et al., 2022, in preparation).

In the Evolutionary Map of the Universe Pilot Survey (area of ∼270 sq. deg.; Norris et al. 2021), we discovered three ORCs by chance, giving a surface density of ORCs that is consistent with finding one in the 120 sq. deg. ASKAP image of the LMC (Pennock et al. 2021). However, J0624–6948 differs from the known single ORCs in three respects: (i) the ORCs have a steeper spectral index than J0624–6948, (ii) J0624–6948's angular size of 196 arcsec is significantly larger than the typical 80 arcsec size of ORCs, (iii) all single ORCs have a central elliptical galaxy, whereas the nearest galaxy to the centre of J0624–6948 is the lenticular galaxy 10.8 arcsec from the centre, discussed in Section 3.1.

Because of these differences, we consider it unlikely (but not impossible) that J0624–6948 is an ORC. Below, we consider several possibilities for its ORC-like formation.

5.1.1 *Precessing jets*

Horton, Krause & Hardcastle (2020) have shown that precessing jets in an 30Dor can display a number of morphologies. In particular, if the jets are seen end-on, they might be observed as one or two circular discs of emission. These might form rings if the precession time-scale is significantly shorter than the source age and the radiative time-scale of the hotspot. However, such exact rings remain hypothetical, as they have not yet been observationally confirmed.

Although, an interesting example of possible precessing jets is seen in the nearby (350 Mpc) ultra-luminous infrared galaxy WISEA J060253.98-710310.0 (Doi et al. 2019), which is a merging pair of spiral galaxies (Filipović et al., in preparation). These authors show that merging spiral galaxies SMBH are most likely responsible for producing spirals of circular (precessing) jets spanning over 600 kpc in length. In this case, one of the two SMBHs is 'disturbing' the jet emission on a regular basis, and switching it off at the same time, creating rings and jet spirals. If observed directly along the line of sight, one would expect to see nearly circular rings. We note a number of other examples that would fit into the category of '30Dor sprinklers' were found by visual inspection of various deep radio survey images, e.g. the Quasi-Stellar Object (QSO) candidate DES J061909.04–555843.7 in the ASKAP image of the merging galaxy cluster system Abell 3391 – Abell 3395 (Brüggen et al. 2021), the QSO SDSS J134545.36 + 533252.3 as seen in the VLA Sky Survey (VLASS) Sky Survey (Lacy et al. 2020), LEDA 783409 (a.k.a. DES J004506.98–250146.8 and WISEA J004506.98–250147.0) in a deep ASKAP image of the NGC 253 region (Koribalski et al., in preparation), and the BL Lac object 2MASX J08120189 + 0237325 (Paiano et al. 2020), as seen in VLASS (Lacy et al. 2020).

If J0624–6948 is caused by a precessing 30Dor, it should have a radio-loud 30Dor in the centre. The nearest candidate is the lenticular galaxy discussed above, 10.8 arcsec from the centre (Section 3.1). The lack of a bright central radio source might be explained if the jet was currently switched off, although that requires that it has only just switched off, but was previously switched on for at least a precession period to illuminate the ring. However, lenticular galaxies do not often host radio 30Dor. Furthermore, the galaxy appears edge-on, so is unlikely to be hosting an end-on radio 30Dor. Furthermore, the redshift of this galaxy is $z \gtrsim 0.7$ (Section 3.1), implying a diameter of the ring of $\gtrsim 1.4$ Mpc. If the precessing jets subtend an angle of 10 degrees at the 30Dor, then this implies a distance between the front and back hotspots of $\gtrsim 8$ Mpc, making this one of the largest radio 30Dors ever observed.

We therefore consider it unlikely that J0624–6948 is caused by precessing jets from an 30Dor.

5.1.2 *Buoyant toroidal structures*

Dynamical evolution of buoyantly rising remnant lobes can produce toroidal structures (Churazov et al. 2001), which will be seen as rings

Downloaded from https://academic.oup.com/mnras/article/512/1/265/6522201 by UNI CATANIA FAC AGRARIA user on 27 February 2025

when viewed end-on. However, the time-scale to evacuate a central cavity is comparable to the sound crossing time, which is of order 200 Myr if the central galaxy is at $z \gtrsim 0.7$. This is much longer than the typical remnant fading time-scale (Shabala et al. 2020). While re-acceleration of remnant plasma is possible, the relatively flat radio spectral index of the J0624–6948 would imply a very strong shock. Therefore, we consider this interpretation less plausible.

5.1.3 Bent-tailed galaxy

Another possibility for an 30Dor origin is that it might be caused by a bent-tailed galaxy. For example, the bent-jets from the narrow-angle tail (NAT) galaxy NGC 1265 (O'Dea & Owen 1986) initially form a semi-circle, but then broaden and merge downstream, creating the large tails characteristic of a NAT galaxy. However, this model suffers from two problems: (a) no tailed galaxy has been observed to form a full circle, (b) no bright radio 30Dor host is found along the J0624–6948 ring. We examined all compact sources along the J0624–6948 ring feature and found no evidence that they could be associated with a host galaxy that would be the source of a twin bent-jet structure. There is a bright X-ray source XMMU J062426.76–694726.3 (Fig. 5) on the north-east rim of the J0624–6948, which is presumably an 30Dor, but although visible at infrared and optical wavelengths, it does not correspond to a radio source, and so appears to be radio-quiet.

5.2 Nearby remnant of a stellar super-flare

What if J0624–6948 is the result of a nearby stellar super-flare(s)? At the NW side of the J0624–6948 ring (Fig. 5), we found the star *Gaia* EDR3 5278760380137682816 (also known as 2MASS J06240216–6948116; RA(J2000) = $06^{h}24^{m}2.151^{s}$ and Dec(J2000) = $-69^{\circ}48'11.64''$).

This object has a very red colour in SMASH DR2 with $(g - i)_0 = 3.24$, which indicates that this star is a foreground M-dwarf (fig. 3 in Wan et al. 2020). In addition, this star is much brighter at longer wavelengths. 2MASS photometry shows that the K-band brightness is 11.9 mag, which is much brighter than the SMASH *i*-band brightness (∼15.5 mag). From *Gaia* EDR3, this star has a proper motion in declination of $\sim 46.086 \pm 0.050$ mas yr^{-1}, plus a small proper motion in RA of $\sim -0.142 \pm 0.048$ mas yr^{-1}; it has a *G*-band magnitude of 16.271, and a parallax of 17.078 ± 0.039 mas, putting it at a distance of 58.5 pc. At this distance, the 196 arcsec circular shell could be a giant coronal mass ejection (CME) that would have a linear diameter of ∼0.186 ly (0.057 pc), and with an assumed expansion velocity of $\upsilon = 50$–500 km s^{-1} (Argiroffi et al. 2019; Namekata et al. 2021) would give an age of ∼56–560 yr. Our modelling suggests this could represent a mass ejection of $\sim 2 \times 10^{22}$ g and an CME energy of $\geq 2 \times 10^{36}$ erg $M/(2 \times 10^{21}\ \mathrm{g})(v_{CME}/(450\ \mathrm{km\ s^{-1}}))^2$. These estimates could be associated with super-flares from young rapidly rotating stars (Notsu et al. 2019). But would the radio continuum emission we see be expected from such a CME? Presently, there is no example of a radio ring around a flare star (or any modelling that suggests there should be).

However, flare stars are known X-ray and radio emitters (Crosley & Osten 2018). For example, a stellar flare on HR 9024 (Argiroffi et al. 2019) has been observed using the High Energy Transmission Grating Spectrometer on *Chandra*. Doppler shifts of hot plasmas (up to 25×10^6 K) from S_{XVI}, S_{XIV}, and Mg_{XII} lines indicate motions with velocities of 50–500 km s^{-1}. Additionally, a blueshift in the O_{VIII} line indicates an upward motion of relatively cool plasma with a velocity of $\upsilon = 90 \pm 30$ km s^{-1}. This is thought to be a CME with a mass of $\sim 10^{21}$ g and 5×10^{34} ergs as detailed in Argiroffi et al. (2019). This represents a major loss of stellar mass but still an order of magnitude smaller than our above estimates.

The fact that the *Gaia* star is clearly detected in the *XMM-Newton* image as a point source (see Table 3) and its position on the rim of J0624–6948 (see Fig. 5), as well as its large proper motion makes this scenario feasible to explore. This may represent quasi-simultaneous flare/burst eruptions (temporally close together). There are several known coherent radio bursts from M-dwarfs (Villadsen & Hallinan 2019). As a radio object, M-dwarfs could have a diverse morphology and the duration of these flare/bursts could range from seconds to hours. They all share strong (40–100 per cent) circular polarization (Villadsen & Hallinan 2019), which we do not see in any of our radio images nor is there a distinctive radio point source at the *Gaia* and/or *XMM-Newton* star position. Villadsen & Hallinan (2019) also showed that no such events resemble solar Type II bursts (often associated with CMEs), but they also could not rule out the occurrence of radio-quiet stellar CMEs.

If this is indeed a nearby remnant of a stellar super-flare (or burst) then one would expect to see detectable proper motions due to the expansion of the ring. We estimate that over a 2-yr period, assuming an expansion velocity of $\upsilon = 50$–500 km s^{-1}, the distance of 58.5 pc and a shell diameter size of 0.057 pc the shell would expand between 0.4 and 5.6 arcsec, which is well within the capabilities of the present generation of radio telescopes. However, it would be strange for the ring not to be concentric around that star as a conservation of momentum would require it to move in the same way unless it moves through a dense medium. Finally, if the circular shell material seen in radio is from a CME, which has high density, we would expect to detect it in various optical lines.

5.3 Planetary nebula

We rule out a PN scenario as an explanation for J0624–6948. If it is at the LMC distance, it would be an order of magnitude larger than any known PN (Filipović et al. 2009; Bojičić et al. 2011; Leverenz et al. 2016, 2017). If of Galactic origin, then prominent IR and optical emission would be seen in any (even shallow) image, which we do not see.

6 WHAT IS J0624–6948?

Multifrequency radio analysis reveals an almost perfectly circular ring radio source J0624–6948 in an unexpected location, in the direction between the LMC and the plane of the MW. At the distance of the LMC, the source size of 47.2 ± 1.0 pc is consistent with an intergalactic SNR interpretation. Various other intrinsic properties, including the spectral index ($\alpha = -0.4 \pm 0.1$) and morphology, are also consistent with an identification as a bilateral SNR. However, the lack of detectable radio polarization is not consistent with such a scenario but also not totally unexpected. The progenitor of SNR J0624–6948 is more likely to be from the outer disc of the LMC, but we cannot rule out a HVS as an origin. At the same time, we favour a type Ia SN over a CCSN because of the location and stellar content of the area around the J0624–6948, as well as a very low (uniform)-ambient density and the lack of morphological features expected for a CCSN of a fast-moving star. If J0624–6948 is an SNR, its most likely distance is 50 kpc and with the upper limit for its X-ray flux we obtain $n_H \lesssim 0.008$ cm^{-3}, thus the SNR would be younger than ∼7100 yr, implying it is in a late ED or early-Sedov phase (Table 4). This would make J0624–6948 an ideal laboratory to

Downloaded from https://academic.oup.com/mnras/article/512/1/265/6522201 by UNI CATANIA FAC AGRARIA user on 27 February 2025

study this evolutionary stage of SNRs in a low-density intergalactic environment.

While J0624–6948 has the morphology of an ORC, it is of larger angular size, has a flatter spectrum, and does not have a prominent central elliptical galaxy.

Another scenario for J0624–6948 would include a precessing 30Dor jet, but the near-perfect symmetry with a complete ring structure, and the lack of a bright radio/optical central source, argue against it, although this could be a result of the 30Dor being in a 'switched-off' mode.

A weak central radio source located 10.8 arcsec from the geometric centre is unlikely to be a central 30Dor engine and even less likely a PWN, as it coincides with a faint edge-on late-type or lenticular (S0) galaxy seen on SMASH optical images. We also note four nearby bright radio sources towards the south-west edges of the J0624–6948 ring – all, most likely, unrelated background objects.

We review other possible ORC etiologies and discuss relevant models. These include its identity as a remnant of a stellar super-flare or ejected bubble shell from the nearby *Gaia* EDR3 5278760380137682816 M-dwarf star, although an unfavourable direction of proper motion, as well as an explanation for asymmetries to the parent star would be required. Finally, we rule out a PN scenario.

In conclusion, our preferred interpretation for the nature of J0624–6948 is an intergalactic SNR that comes from a single-degenerate type Ia SN located in the far eastern outskirts of the LMC, which expands into a rarefied, intergalactic environment.

ACKNOWLEDGEMENTS

The Australian SKA Pathfinder is a part of the Australia Telescope National Facility, which is managed by Australian Commonwealth Scientific and Industrial Research Organisation (CSIRO). Operation of ASKAP is funded by the Australian Government with support from the National Collaborative Research Infrastructure Strategy. ASKAP uses the resources of the Pawsey Supercomputing Centre. Establishment of ASKAP, the Murchison Radio-astronomy Observatory, and the Pawsey Supercomputing Centre are initiatives of the Australian Government, with support from the Government of Western Australia and the Science and Industry Endowment Fund. We acknowledge the Wajarri Yamatji people as the traditional owners of the Observatory site. The ATCA is a part of the Australia Telescope National Facility, which is funded by the Australian Government for operation as a National Facility managed by CSIRO. This research has made use of the WIFES, operated by the Jet Propulsion Laboratory, California Institute of Technology, under contract with the National Aeronautics and Space Administration; and WIFES is also a joint project with the University of California, Los Angeles. Additionally, this research has made use of the SIMBAD database, operated at CDS, Strasbourg, France (Wenger et al. 2000), SAOIMAGE DS9, NASA's Astrophysics Data System Bibliographic Services, VIZIER catalogue access tool, CDS, Strasbourg, France. The original description of the VIZIER service was published in Ochsenbein, Bauer & Marcout (2000).

HA has benefited from grant CIIC 174/2021 of Universidad de Guanajuato, Mexico. DU acknowledges Ministry of Education, Science, and Technological Development of the Republic of Serbia through the contract No. 4451-03-9/2021-14/200104. We thank B. Gaensler for constructive comments and suggestions. Robert Brose acknowledges funding from an Irish Research Council Starting Laureate Award (IRCLA/2017/83). We thank an anonymous referee for comments and suggestions that greatly improved our paper.

DATA AVAILABILITY

Data that support the plots/images within this paper and other findings of this study are available from the corresponding author upon reasonable request. The ASKAP data used in this article are available through the CSIRO ASKAP Science Data Archive (CASDA) and ATCA data via the Australia Telescope Online Archive (ATOA).

REFERENCES

Acero F., Ballet J., Decourchelle A., 2007, A&A, 475, 883
Ajello M. et al., 2020, ApJ, 892, 105
Alsaberi R. Z. E. et al., 2019, Ap&SS, 364, 204
Anderson M. C., Keohane J. W., Rudnick L., 1995, ApJ, 441, 300
Argiroffi C. et al., 2019, Nature Astron., 3, 742
Arnaud K. A., 1996, in Jacoby G. H., Barnes J., eds, ASP Conf. Ser., Vol. 101, Astronomical Data Analysis Software and Systems V. Astron. Soc. Pac., San Francisco, p. 17
Balucinska-Church M., McCammon D., 1992, ApJ, 400, 699
Becker W., Hurley-Walker N., Weinberger C., Nicastro L., Mayer M. G. F., Merloni A., Sanders J., 2021, A&A, 648, A30
Besla G., Martínez-Delgado D., van der Marel R. P., Beletsky Y., Seibert M., Schlafly E. F., Grebel E. K., Neyer F., 2016, ApJ, 825, 20
Bojičić I. S., Parker Q. A., Filipović M. D., Frew D. J., 2011, MNRAS, 412, 223
Boubert D., Erkal D., Evans N. W., Izzard R. G., 2017, MNRAS, 469, 2151
Boubert D., Erkal D., Gualandris A., 2020, MNRAS, 497, 2930
Bozzetto L. M., Filipović M. D., Urošević D., Kothes R., Crawford E. J., 2014, MNRAS, 440, 3220
Bozzetto L. M. et al., 2017, ApJS, 230, 2
Brantseg T., McEntaffer R. L., Bozzetto L. M., Filipović M., Grieves N., 2014, ApJ, 780, 50
Brown W. R., 2015, ARA&A, 53, 15
Brüggen M. et al., 2021, A&A, 647, A3
Cendes Y., Gaensler B. M., Ng C. Y., Zanardo G., Staveley-Smith L., Tzioumis A. K., 2018, ApJ, 867, 65
Choi J., Dotter A., Conroy C., Cantiello M., Paxton B., Johnson B. D., 2016, ApJ, 823, 102
Chomiuk L. et al., 2018, Astron. Telegram, 11610, 1
Churazov E., Brüggen M., Kaiser C. R., Böhringer H., Forman W., 2001, ApJ, 554, 261
Churazov E. M., Khabibullin I. I., Bykov A. M., Chugai N. N., Sunyaev R. A., Zinchenko I. I., 2021, MNRAS, 507, 971
Collier J. D. et al., 2018, MNRAS, 477, 578
Conroy C., et al., 2021, Nature, 592, 534
Crawford T. M. et al., 2016, ApJS, 227, 23
Crosley M. K., Osten R. A., 2018, ApJ, 856, 39
Cullinane L. R. et al., 2020, MNRAS, 497, 3055
De Horta A. Y. et al., 2014, Serb. Astron. J., 189, 41
Dickey J. M., Lockman F. J., 1990, ARA&A, 28, 215
Dickinson C., 2018, Galaxies, 6, 56
Doi R., Nakagawa T., Isobe N., Baba S., Yano K., Yamagishi M., 2019, PASJ, 71, 26
Dotter A., 2016, ApJS, 222, 8
Ducci L., Kavanagh P. J., Sasaki M., Koribalski B. S., 2014, A&A, 566, A115
Ducci L. et al., 2020, Astron. Telegram, 13545, 1
Edelmann H., Napiwotzki R., Heber U., Christlieb N., Reimers D., 2005, ApJ, 634, L181
Eldridge J. J., Langer N., Tout C. A., 2011, MNRAS, 414, 3501
Erkal D., Boubert D., Gualandris A., Evans N. W., Antonini F., 2019, MNRAS, 483, 2007
Evans F. A., Renzo M., Rossi E. M., 2020, MNRAS, 497, 5344
Evans F. A., Marchetti T., Rossi E. M., Baggen J. F. W., Bloot S., 2021, MNRAS, 507, 4997
Filipović M. D., Tothill N. F. H., 2021b, Principles of Multimessenger Astronomy. IOP Publishing, https://books.google.com.au/books?id=DjvPzgEACAAJ

Downloaded from https://academic.oup.com/mnras/article/512/1/265/6522201 by UNI CATANIA FAC AGRARIA user on 27 February 2025

Filipović M. D., Haynes R. F., White G. L., Jones P. A., 1998, A&AS, 130, 421
Filipović M. D. et al., 2009, MNRAS, 399, 769
Filipović M. D. et al., 2021, MNRAS, 507, 2885
Filipović M. D., Tothill N. F. H., 2021a, Multimessenger Astronomy in Practice. Institute of Physics Publishing, https://dx.doi.org/10.1088/2514-3433/ac2256
For B.-Q. et al., 2018, MNRAS, 480, 2743
Fragione G., Gualandris A., 2019, MNRAS, 489, 4543
Freundlich J., Maoz D., 2021, MNRAS, 502, 5882
Gaensler B. M., 1998, ApJ, 493, 781
Gaia Collaboration, 2021, A&A, 649, A1
Galvin T. J., Filipović M. D., 2014, Serb. Astron. J., 189, 15
Geier S. et al., 2015, Science, 347, 1126
Gooch R., 1995, in Shaw R. A., Payne H. E., Hayes J. J. E., eds, ASP Conf. Ser., Vol. 77, Astronomical Data Analysis Software and Systems IV. Astron. Soc. Pac., San Francisco, p. 144
Gualandris A., Portegies Zwart S., 2007, MNRAS, 376, L29
Haberl F., Sturm R., Filipović M. D., Pietsch W., Crawford E. J., 2012, A&A, 537, L1
Hakobyan A. A. et al., 2017, MNRAS, 471, 1390
Hancock P. J., Trott C. M., Hurley-Walker N., 2018, Publ. Astron. Soc. Aust., 35, e011
Harvey-Smith L., Gaensler B. M., Kothes R., Townsend R., Heald G. H., Ng C. Y., Green A. J., 2010, ApJ, 712, 1157
HI4PI Collaboration, 2016, A&A, 594, A116
Hills J. G., 1988, Nature, 331, 687
Hirsch H. A., Heber U., O'Toole S. J., Bresolin F., 2005, A&A, 444, L61
Horton M. A., Krause M. G. H., Hardcastle M. J., 2020, MNRAS, 499, 5765
Hurley-Walker N. et al., 2019a, Publ. Astron. Soc. Aust., 36, e045
Hurley-Walker N. et al., 2019b, Publ. Astron. Soc. Aust., 36, e048
Irrgang A., Kreuzer S., Heber U., 2018, A&A, 620, A48
Irrgang A., Dimpel M., Heber U., Raddi R., 2021, A&A, 646, L4
Jarrett T. H. et al., 2012, AJ, 144, 68
Jarrett T. H., Cluver M. E., Brown M. J. I., Dale D. A., Tsai C. W., Masci F., 2019, ApJS, 245, 25
Kavanagh P. J. et al., 2016, A&A, 586, A4
Kavanagh P. J., Sasaki M., Filipović M. D., Points S. D., Bozzetto L. M., Haberl F., Maggi P., Maitra C., 2021, preprint (arXiv:2111.00446)
Khokhlov A., Mueller E., Hoeflich P., 1993, A&A, 270, 223
Koposov S. E. et al., 2020, MNRAS, 491, 2465
Koribalski B. S., Norris R. P., Andernach H., Rudnick L., Shabala S., Filipović M., Lenc E., 2021, MNRAS, 505, L11
Kothes R., Reich W., 2001, A&A, 372, 627
Kothes R., Furst E., Reich W., 1998, A&A, 331, 661
Kothes R., Fedotov K., Foster T. J., Uyanıker B., 2006, A&A, 457, 1081
Kothes R., Reich P., Foster T. J., Reich W., 2017, A&A, 597, A116
Kothes R., Reich W., Safi-Harb S., Guest B., Reich P., Fürst E., 2020, MNRAS, 496, 723
Lacy M. et al., 2020, PASP, 132, 035001
Leahy D. A., 2017, ApJ, 837, 36
Leahy D. A., Ranasinghe S., 2018, ApJ, 866, 9
Leahy D., Wang Y., Lawton B., Ranasinghe S., Filipović M., 2019, AJ, 158, 149
Leahy D. A., Ranasinghe S., Gelowitz M., 2020, ApJS, 248, 16
Leverenz H., Filipović M. D., Bojičić I. S., Crawford E. J., Collier J. D., Grieve K., Drašković D., Reid W. A., 2016, Ap&SS, 361, 108
Leverenz H., Filipović M. D., Vukotić B., Urošević D., Grieve K., 2017, MNRAS, 468, 1794
Lopez L. A., Ramirez-Ruiz E., Huppenkothen D., Badenes C., Pooley D. A., 2011, ApJ, 732, 114
Luken K. J. et al., 2020, MNRAS, 492, 2606
Maggi P. et al., 2016, A&A, 585, A162
Maggi P. et al., 2019, A&A, 631, A127
Maitra C., Haberl F., Maggi P., Kavanagh P. J., Vasilopoulos G., Sasaki M., Filipović M. D., Udalski A., 2021, MNRAS, 504, 326
Maoz D., Mannucci F., 2012, Publ. Astron. Soc. Aust., 29, 447
Marocco F. et al., 2021, ApJS, 253, 8
McKee C. F., Truelove J. K., 1995, Phys. Rep., 256, 157
Meyer D. M. A., Langer N., Mackey J., Velázquez P. F., Gusdorf A., 2015, MNRAS, 450, 3080
Meyer D. M. A., Pohl M., Petrov M., Oskinova L., 2021, MNRAS, 502, 5340
Millar W. C., White G. L., Filipović M. D., 2012, Serb. Astron. J., 184, 19
Namekata K. et al., 2021, Nature Astron., preprint (arXiv:2112.04808)
Neunteufel P., 2020, A&A, 641, A52
Nidever D. L. et al., 2021, AJ, 161, 74
Nikolaev S., Drake A. J., Keller S. C., Cook K. H., Dalal N., Griest K., Welch D. L., Kanbur S. M., 2004, ApJ, 601, 260
Norris R. P. et al., 2021, Publ. Astron. Soc. Aust., 38, e046
Norris R. P., Crawford E., Macgregor P., 2021a, Galaxies, 9, 83
Norris R. P. et al., 2021b, Publ. Astron. Soc. Aust., 38, e003
Notsu Y. et al., 2019, ApJ, 876, 58
O'Dea C. P., Owen F. N., 1986, ApJ, 301, 841
Ochsenbein F., Bauer P., Marcout J., 2000, A&AS, 143, 23
Onken C. A. et al., 2019, Publ. Astron. Soc. Aust., 36, e033
Paiano S., Falomo R., Treves A., Scarpa R., 2020, MNRAS, 497, 94
Pakmor R., Kromer M., Taubenberger S., Springel V., 2013, ApJ, 770, L8
Pavlovic M. Z., Dobardzic A., Vukotic B., Urosevic D., 2014, Serb. Astron. J., 189, 25
Pavlović M. Z., Urošević D., Arbutina B., Orlando S., Maxted N., Filipović M. D., 2018, ApJ, 852, 84
Pejcha O., Prieto J. L., 2015, ApJ, 806, 225
Pennock C. M. et al., 2021, MNRAS, 506, 3540
Petruk O., Kuzyo T., Orlando S., Pohl M., Brose R., 2021, MNRAS, 505, 755
Piatti A. E., Geisler D., 2013, AJ, 145, 17
Pietrzyński G. et al., 2019, Nature, 567, 200
Platais I. et al., 2018, AJ, 156, 98
Przybilla N., Nieva M. F., Heber U., Firnstein M., Butler K., Napiwotzki R., Edelmann H., 2008, A&A, 480, L37
Raddi R. et al., 2019, MNRAS, 489, 1489
Ranasinghe S., Leahy D., 2019, J. High Energy Phys. Grav. Cosmol., 5, 907
Reynolds S. P., Gaensler B. M., Bocchino F., 2012, Space Sci. Rev., 166, 231
Reynoso E. M., Hughes J. P., Moffett D. A., 2013, AJ, 145, 104
Roper Q. et al., 2018, MNRAS, 479, 1800
Rudnick L., 2002, PASP, 114, 427
Sadeh I., Abdalla F. B., Lahav O., 2016, PASP, 128, 104502
Sault R. J., Teuben P. J., Wright M. C. H., 1995, in Shaw R. A., Payne H. E., Hayes J. J. E., eds, ASP Conf. Ser., Vol. 77, Astronomical Data Analysis Software and Systems IV. Astron. Soc. Pac., San Francisco, p. 433
Schlafly E. F., Finkbeiner D. P., 2011, ApJ, 737, 103
Schlafly E. F., Meisner A. M., Green G. M., 2019, ApJS, 240, 30
Shabala S. S., Jurlin N., Morganti R., Brienza M., Hardcastle M. J., Godfrey L. E. H., Krause M. G. H., Turner R. J., 2020, MNRAS, 496, 1706
Shen K. J. et al., 2018, ApJ, 865, 15
Strüder L. et al., 2001, A&A, 365, L18
Sun X. H., Reich W., Wang C., Han J. L., Reich P., 2011, A&A, 535, A64
Truelove J. K., McKee C. F., 1999, ApJS, 120, 299
Turner M. J. L. et al., 2001, A&A, 365, L27
Turtle A. J., Pugh J. F., Kenderdine S., Pauliny-Toth I. I. K., 1962, MNRAS, 124, 297
Urošević D., 2020, Nature Astron., 4, 910
Villadsen J., Hallinan G., 2019, ApJ, 871, 214
Vukotić B., Ćiprijanović A., Vučetić M. M., Onić D., Urošević D., 2019, Serb. Astron. J., 199, 23
Wan Z., Guglielmo M., Lewis G. F., Mackey D., Ibata R. A., 2020, MNRAS, 492, 782
Webbink R. F., 1984, ApJ, 277, 355
Wenger M. et al., 2000, A&AS, 143, 9
West J. L., Safi-Harb S., Jaffe T., Kothes R., Landecker T. L., Foster T., 2016, A&A, 587, A148
West J. L., Safi-Harb S., Ferrand G., 2017, A&A, 597, A121
West J. L., Landecker T. L., Gaensler B. M., Jaffe T., Hill A. S., 2021, ApJ, 923, 58
Whelan J., Iben, Icko J., 1973, ApJ, 186, 1007
Wilms J., Allen A., McCray R., 2000, ApJ, 542, 914
Xiao L., Fürst E., Reich W., Han J. L., 2008, A&A, 482, 783

Downloaded from https://academic.oup.com/mnras/article/512/1/265/6522201 by UNI CATANIA FAC AGRARIA user on 27 February 2025

Yew M. et al., 2021, MNRAS, 500, 2336
Zinn P. C., Grunden P., Bomans D. J., 2011, A&A, 536, A103

APPENDIX A: J0624–6948 AND THE UNIFIED SNR EVOLUTION MODEL

In addition to McKee & Truelove (1995), we also explore the 'unified SNR evolution models' (Leahy & Ranasinghe 2018; Truelove & McKee 1999), using the software SNRPY from Leahy et al. (2019), a SN explosion energy of 0.5×10^{51} erg (Leahy 2017; Leahy et al. 2020), and type Ia SN ejecta mass of 1.4 $M_{\odot}$. For ejecta with a power-law envelope with index 7 and depending on the above range of the local density (10^{-1}–10^{-4} cm^{-3}), the SNR would reach a radius of 23.8 pc at an age of 2300–25 000 yr and shock velocities of 6050 km s^{-1} to 400 km s^{-1} (see Table A1). If as old as 25 000 yr, it would still be in the Sedov phase. However, a more likely scenario has an ambient density of ∼0.001–0.01 cm^{-3} which would argue for an SNR of age 4000–9000 yrthat is still in early (4000 yr) to late (9000 yr) transition from the ejecta-dominated (ED) phase to the Sedov phase.

As additional test, we placed J0624–6948 at various distances from 5 to 70 kpc, which changed the radius from 2.4 to 33.3 pc (Table A1). For those distances, we initially set the ISM density to 0.01 cm^{-3}, which is not extreme for an SNR. From the 47 Galactic SNRs modelled by Leahy et al. (2020), four have density <0.01 cm^{-3}. The models for a density of 0.01 cm^{-3} predict somewhat brighter SNRs than the limit given by the X-ray flux upper limits. By adjusting the ISM density to range from 0.0094 cm^{-3} (for 20 kpc distance) to 0.0083 cm^{-3} (for 70 kpc distance), the unified SNR evolution model (; Truelove & McKee 1999; Leahy et al. 2019) fluxes are equal to the upper limits. Thus, we set the density to 0.008 cm^{-3} to be below the X-ray upper limits that produces estimated ages from 113 to 17 200 yr (see Table A1). These are faint in X-rays, consistent with the X-ray limits (see next paragraph). However, for the nearest and youngest of these (ages 113 and 378 yr), the SNe would have been almost certainly observed historically because they are bright type Ia at high Galactic latitude where there is no significant extinction. For distances ≥20 kpc, the age is large enough that they could have escaped the historical record. This, together with paucity of progenitors in the 20–40 kpc distance range (see Section 4.1), would also suggest that the positioning of J0624–6948 as an SNR is more likely to be at the LMC distance of ∼50 kpc.

[1]*School of Science, Western Sydney University, Locked Bag 1797, Penrith South DC, NSW 2751, Australia*
[2]*CSIRO Space & Astronomy, PO Box 76, Epping, NSW 1710, Australia*
[3]*Minnesota Institute for Astrophysics, School of Physics and Astronomy, University of Minnesota, 116 Church Street SE, Minneapolis, MN 55455, USA*
[4]*Department of Physics and Astronomy, University of Calgary, University of Calgary, Calgary, Alberta, T2N 1N4, Canada*
[5]*Institut für Astronomie und Astrophysik, Kepler Center for Astro and Particle Physics, Universität Tübingen, Sand 1, D-72076 Tübingen, Germany*
[6]*ISDC Data Center for Astrophysics, Université de Genève, 16 chemin d'Écogia, CH-1290 Versoix, Switzerland*
[7]*Dominion Radio Astrophysical Observatory, Herzberg Astronomy and Astrophysics, National Research Council Canada, PO Box 248, Penticton, BC V2A 6J9, Canada*
[8]*Departamento de Astronomía, DCNE, Universidad de Guanajuato, Cjón, de Jalisco s/n, Col. Valenciana, Guanajuato CP 36023, Gto., Mexico*
[9]*Dublin Institute for Advanced Studies, Astronomy & Astrophysics Section, 31 Fitzwilliam Place, D02 XF86 Dublin 2, Ireland*
[10]*University of Potsdam, Institute of Physics and Astronomy, D-14476 Potsdam, Germany*
[11]*The Inter-University Institute for Data Intensive Astronomy (IDIA), Department of Astronomy, University of Cape Town, Rondebosch 7701, South Africa*
[12]*Research School of Astronomy and Astrophysics, Australian National University, Canberra 2611, ACT, Australia*
[13]*International Centre for Radio Astronomy Research, Curtin University, Bentley, WA 6102, Australia*
[14]*Max-Planck-Institut für extraterrestrische Physik, Gießenbachstraße 1, D-85748 Garching, Germany*
[15]*Remeis Observatory and ECAP, Universität Erlangen-Nürnberg, Sternwartstraße 7, D-96049 Bamberg, Germany*

Table A1. J0624–6948 as an SNR of type Ia at various distances (radius) and various ISM densities ($n_{\rm H} = 10^{-1} - 10^{-4}$ cm^{-3}). Based on the model of Leahy & Ranasinghe (2018), we assume an SN explosion energy of 0.5×10^{51} erg and type Ia SN ejecta mass of 1.4 $M_{\odot}$. Column 6 lists the emission-measure-weighted shocked gas electron temperature, Column 7 the emission measure (EM), Column 8 the X-ray luminosity (L_X), and Column 9 the swept-up mass (M_{sw}). For $n_{\rm H} = 0.008$ cm^{-3}, the reverse shock reaches the centre at 10 800 yr for all cases.

(1) Distance (kpc)	(2) Radius (pc)	(3) $n_{\rm H}$ (cm^{-3})	(4) Age (yr)	(5) Shock υ (km s^{-1})	(6) Shock T_e (K)	(7) EM (cm^{-3})	(8) L_X (erg s^{-1})	(9) M_{sw} ($M_{\odot}$)	(10) Comment
50	23.8	0.1	25000	400	4.5×10^6	4.4×10^{58}	2.2×10^{35}	175	Sedov phase, reverse shock reaches centre at 4630 yr
50	23.8	0.01	8600	1250	1.0×10^7	4.5×10^{56}	4.9×10^{33}	17.5	Late transition from ED phase, reverse shock reaches centre at 9980 yr
50	23.8	0.001	4100	3400	1.7×10^7	4.8×10^{54}	8.8×10^{31}	1.75	Early transition from ED phase, reverse shock reaches centre at 21 500 yr
50	23.8	0.0001	2300	6050	3.4×10^7	1.0×10^{53}	2.4×10^{30}	0.175	ED phase, reverse shock reaches centre at 46 300 yr
5	2.4	0.008	113	11780	1.2×10^8	5.6×10^{53}	1.8×10^{31}	0.014	ED phase
10	4.7	0.008	378	7019	5.0×10^7	4.5×10^{54}	1.3×10^{32}	0.114	ED phase
20	9.5	0.008	1390	4010	3.6×10^7	2.7×10^{55}	8.1×10^{32}	0.915	ED phase
30	14.3	0.008	2830	2960	2.5×10^7	6.8×10^{55}	1.2×10^{33}	3.12	Early transition from ED phase
40	19.0	0.008	4900	1950	1.7×10^7	1.5×10^{56}	2.0×10^{33}	7.32	Mid transition from ED phase
50	23.8	0.008	7900	1390	1.3×10^7	2.9×10^{56}	3.2×10^{33}	14.0	Late transition from ED phase
60	28.5	0.008	11 900	1060	1.1×10^7	4.9×10^{56}	4.8×10^{33}	24.7	Sedov phase
70	33.3	0.008	17 200	840	9.8×10^6	7.8×10^{56}	6.8×10^{33}	39.4	Sedov phase

Downloaded from https://academic.oup.com/mnras/article/512/1/265/6522201 by UNI CATANIA FAC AGRARIA user on 27 February 2025

[16]*Australian Astronomical Optics, AAO-Macquarie, Faculty of Science and Engineering, Macquarie University, 105 Delhi Rd, North Ryde, NSW 2113, Australia*
[17]*INAF – Osservatorio Astrofisico di Catania, via Santa Sofia 78, I-95123 Catania, Italia*
[18]*Department of Astronomy, University of Cape Town, Private Bag X3, Rondebosch 7701, South Africa*
[19]*School of Cosmic Physics, Dublin Institute for Advanced Studies, 31 Fitzwilliam Place, Dublin 2, Ireland*
[20]*Observatoire Astronomique de Strasbourg, Université de Strasbourg, CNRS, 11 rue de l'Université, F-67000 Strasbourg, France*
[21]*Lennard-Jones Laboratories, Keele University, Staffordshire ST5 5BG, UK*
[22]*Cerro Tololo Inter-American Observatory/NSF's NOIRLab, Casilla 603, La Serena, Chile*
[23]*School of Physical Sciences, The University of Adelaide, Adelaide 5005, Australia*
[24]*Department of Physics and Astronomy, University of Manitoba, Winnipeg, MB R3T 2N2, Canada*
[25]*National Astronomical Observatory of Japan, Mitaka, Tokyo 181-8588, Japan*
[26]*School of Natural Sciences, University of Tasmania, Private Bag 37, Hobart 7001, Australia*
[27]*Department of Astronomy, Faculty of Mathematics, University of Belgrade, Studentski trg 16, 11000 Belgrade, Serbia*
[28]*Isaac Newton Institute of Chile, Yugoslavia Branch*
[29]*Dunlap Institute for Astronomy and Astrophysics, University of Toronto, Toronto, ON M5S 3H4, Canada*
[30]*Sydney Institute for Astronomy, School of Physics, The University of Sydney, Sydney, New South Wales, Australia*

This paper has been typeset from a TEX/LATEX file prepared by the author.

Downloaded from https://academic.oup.com/mnras/article/512/1/265/6522201 by UNI CATANIA FAC AGRARIA user on 27 February 2025